Microscale optoelectronic infrared-to-visible upconversion devices and their use as injectable light sources

He Ding[a,1], Lihui Lu[b,c,1], Zhao Shi[a], Dan Wang[d], Lizhu Li[a], Xichen Li[e], Yuqi Ren[b], Changbo Liu[a], Dali Cheng[a], Hoyeon Kim[f], Noel C. Giebink[f], Xiaohui Wang[g], Lan Yin[d], Lingyun Zhao[d], Minmin Luo[b,c], and Xing Sheng[a,2]

[a]Department of Electronic Engineering, Beijing National Research Center for Information Science and Technology, Tsinghua University, 100084 Beijing, China; [b]National Institute of Biological Sciences, 102206 Beijing, China; [c]School of Life Sciences, Tsinghua University, 100084 Beijing, China; [d]School of Materials Science and Engineering, Tsinghua University, 100084 Beijing, China; [e]Department of Electrical and Computer Engineering, University of Texas at Austin, Austin, TX 78712; [f]Department of Electrical Engineering, The Pennsylvania State University, University Park, PA 16802; and [g]Tianjin Zhonghuan Neolight Technology Co., Ltd., 120111 Tianjin, China

Edited by John A. Rogers, Northwestern University, Evanston, IL, and approved May 16, 2018 (received for review February 5, 2018)

Optical upconversion that converts infrared light into visible light is of significant interest for broad applications in biomedicine, imaging, and displays. Conventional upconversion materials rely on nonlinear light-matter interactions, exhibit incidence-dependent efficiencies, and require high-power excitation. We report an infrared-to-visible upconversion strategy based on fully integrated microscale optoelectronic devices. These thin-film, ultraminiaturized devices realize near-infrared (~810 nm) to visible [630 nm (red) or 590 nm (yellow)] upconversion that is linearly dependent on incoherent, low-power excitation, with a quantum yield of ~1.5%. Additional features of this upconversion design include broadband absorption, wide-emission spectral tunability, and fast dynamics. Encapsulated, free-standing devices are transferred onto heterogeneous substrates and show desirable biocompatibilities within biological fluids and tissues. These microscale devices are implanted in behaving animals, with in vitro and in vivo experiments demonstrating their utility for optogenetic neuromodulation. This approach provides a versatile route to achieve upconversion throughout the entire visible spectral range at lower power and higher efficiency than has previously been possible.

upconversion | optoelectronics | optogenetics

The photon upconversion process converts multiple low-energy photons into a higher energy photon via so-called anti-Stokes emission (1–4), gathering enormous interest in many applications, including biological imaging (5–7), solar energy harvesting (8–11), infrared (IR) sensing (12, 13), displays (14), and solid-state cooling (15). In particular, designed upconversion materials and structures with capabilities of converting IR photons within the "biological transparency window" (~800–1,000 nm) to visible ones are of critical importance to deep-tissue light delivery for biomedical diagnosis and treatment (16–19). State-of-the-art upconversion techniques commonly rely on anti-Stokes mechanisms, including two-photon absorption, second-harmonic generation, and other transition schemes like excited-state absorption and energy transfer upconversion (3, 4, 20–23). However, such processes are typically nonlinear and require coherent or high excitation power (typically laser sources), exhibiting narrow-band and polychromatic excitations and emissions, low and illumination-dependent efficiencies (0.001~1%), and slow responses (μs to ms) (4). Recently reported upconversion materials based on triplet-triplet annihilation present relatively high quantum yields (>1%), but these materials are usually susceptible to oxygen and render small anti-Stokes shifts (22, 23). An alternative upconversion approach involves physically connected or bonded photodetectors and light-emitting devices, with external circuits or power sources to compensate the energy difference and obtain high gains (12, 13, 24). Such device schemes provide viable solutions to IR imaging; however, bulky chips and circuits create challenges for further miniaturization.

In this article, we present materials and device concepts to overcome these issues, by exploiting thin-film, ultracompact, optoelectronic upconversion devices based on semiconductor heterostructures. Through photon–"free electron"–photon processes, such concepts eliminate the constraints of conventional nonlinear upconversion approaches. Fabricated microscale devices realize self-powered IR-to-visible upconversion, with a linear response (quantum yield >1%) under incoherent low-power excitation (as low as 10 mW/cm^2). Additionally, the upconverting devices exhibit monochromatic emission [630 nm (red) or 590 nm (yellow)], broadband sensitivity (400–900 nm), and fast transient decays (lifetime, 47 ns). Integrated with biocompatible encapsulates and substrates, these upconversion devices can be implanted into subdermal tissues and demonstrate both in vitro and in vivo light delivery and neural interrogation.

Significance

Materials and devices that upconvert photons from low to high frequencies are of tremendous interest for broad applications in bio- and chemical sensing, infrared imaging, display, and photovoltaics. Here we develop self-powered, micrometer-scale optoelectronic upconversion devices for infrared-to-visible photon upconversion. The realized microscale optoelectronic device exhibits a practical efficiency of 1.5% under incoherent low-power illumination, with emission intensity linearly dependent on excitation. Other remarkable advances over conventional approaches include broadband absorption, wide-emission spectral tunability (red, yellow, and blue), and fast dynamics. Encapsulated ultraminiaturized devices can be implanted into subdermal tissues and provide stable operation in behaving animals. Demonstrations of optogenetic stimulation in living animals present their potential for biomedical uses.

Author contributions: H.D., L.Y., L.Z., M.L., and X.S. designed research; H.D., L. Lu, Z.S., D.W., L. Li, X.L., Y.R., C.L., D.C., H.K., N.C.G., X.W., and X.S. performed research; X.S. developed the concepts and performed theoretical analysis; H.D., Z.S., L. Li, X.L., C.L., H.K., N.C.G., X.W. and X.S. performed material and device design, fabrication, and characterization; H.D., D.C., and X.S. performed the simulations; H.D., L. Lu, Z.S., D.W., Y.R., L.Y., L.Z., M.L. and X.S. designed and performed biological experiments; H.D., L. Lu, and X.S. analyzed data; and H.D. and X.S. wrote the paper in consultation with the other authors.

The authors declare no conflict of interest.

This article is a PNAS Direct Submission.

[1]H.D. and L. Lu contributed equally to this work.

[2]To whom correspondence should be addressed. Email: xingsheng@tsinghua.edu.cn.

This article contains supporting information online at www.pnas.org/lookup/suppl/doi:10.1073/pnas.1802064115/-/DCSupplemental.

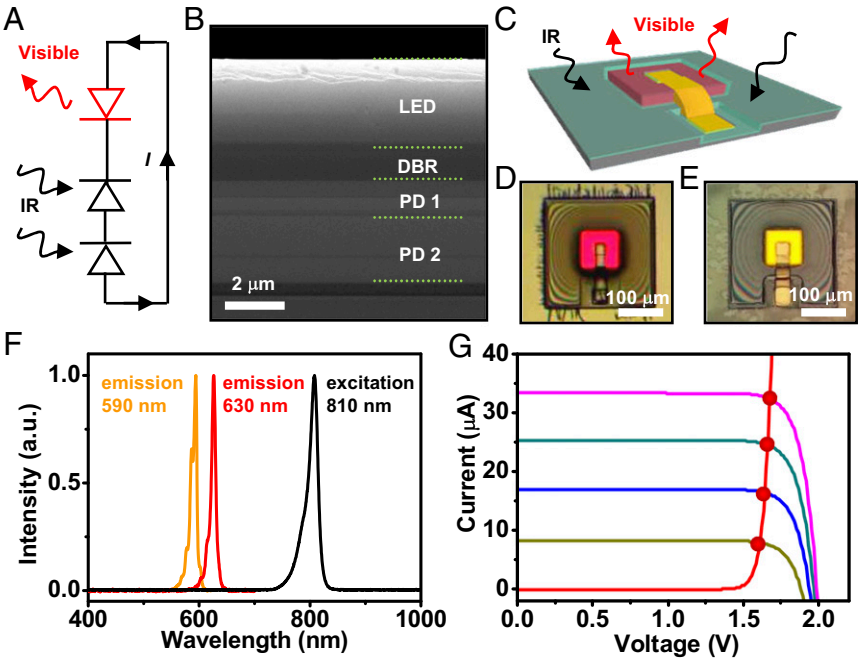

Fig. 1. Schematic illustrations and images of microscale IR-to-visible upconversion devices and their optoelectronic properties. (*A*) The operational principle of the upconversion device design, in which serially connected photodiodes absorb IR light to drive a visible LED. (*B*) SEM image (cross-sectional view) of the epitaxial multilayer stack composed of one layer of a GaInP or AlGaInP LED, one layer of a DBR, and one layer for a GaAs DJPD on a GaAs substrate. (*C*) Schematic illustration of the fabricated upconversion device (tilted view), with the patterned LED (red color) and DJPD (gray color) connected by the deposited metal contact (yellow color) and encapsulated by SU-8 (green color). (*D* and *E*) Microscopic image (top view) of representative upconversion devices with red (*D*) and yellow (*E*) emissions under IR excitation. (*F*) Emission spectra of the excitation source (an 810-nm IR LED), the IR-to-red and the IR-to-yellow upconversion devices with peaks at 630 nm and 590 nm, respectively. (*G*) Current–voltage curves of the two components in the upconversion device: the GaInP red LED (red curve) and the GaAs DJPD under IR illumination with various power densities (21, 43, 60, and 79 mW/cm^2). DBR, distributed Bragg reflector.

Results

Demonstration of Microscale, IR-to-Visible Upconversion Devices. Fig. 1*A* schematically illustrates our proposed upconversion strategy based on fully integrated microscale optoelectronic devices. Here photovoltaic diodes (PDs) capture low-energy IR photons, providing photogenerated currents and voltages that drive a light-emitting diode (LED) to emit high-energy visible photons. Since a single IR PD made by low-bandgap semiconductors cannot supply enough photovoltage to turn on the visible LED, two or more PDs are serially connected to compensate the voltage difference and retain energy conservation for IR-to-visible upconversion. Detailed balance analysis suggests that such a combined "photon-to-electron" and "electron-to-photon" process is able to approach the thermodynamic limits of photon energy conversion (*SI Appendix*, Figs. S1 and S2). Fig. 1*B* depicts a cross-sectional SEM image of the designed device structure, which is based on a serially connected double junction (DJ) gallium arsenide (GaAs) PD (bandgap ∼1.4 eV) and an aluminum gallium indium phosphide (AlGaInP)-based visible LED, which can be $Ga_{0.5}In_{0.5}P$ for red emission (bandgap ∼1.9 eV) or $Al_{0.15}Ga_{0.35}In_{0.5}P$ for yellow emission (bandgap ∼2.1 eV) (more details in *SI Appendix*, Fig. S3 and Table S1). Each junction in the GaAs DJPD is designed to realize current matching and maximum operating efficiency at ∼810 nm, with a thin-film GaAs tunnel junction in between. The top AlGaInP LED is connected to the GaAs PDs by a conductive AlInP/AlGaInP-based distributed Bragg reflector for improved efficiency at corresponding (red or yellow) emission wavelengths (*SI Appendix*, Fig. S4). Formed by metal organic chemical vapor deposition, the multilayered device stack (∼9-μm thick) is lattice matched and epitaxially grown on a GaAs substrate with an $Al_{0.95}Ga_{0.05}As$-based sacrificial layer that can be selectively eliminated later for thin-film device release. Followed by lithographic etching and deposition processes (*SI Appendix* and *SI Appendix*, Fig. S5), the top p-type gallium phosphide layer of the AlGaInP LED and the bottom p-GaAs layer of the GaAs PD are connected by metalized contacts (Fig. 1*C*).

The finalized upconversion device has lateral dimensions of 220 × 220 μm^2 and an active layer thickness of 9 μm, emitting red light at ∼630 nm (Fig. 1*D*) or yellow light at ∼590 nm (Fig. 1*E*) under incoherent illumination provided by an IR LED at ∼810 nm with a power density as low as 2 mW/cm^2, showing anti-Stokes shifts of 0.4 and 0.6 eV for IR-to-red and IR-to-yellow upconversions, respectively (Fig. 1*F*). Unlike typical rare-earth–based upconverting materials with polychromatic emissive spectra (5, 9), the light output from our upconversion devices is purely monochromatic and widely tunable based on semiconductor compositions, which is advantageous for applications like chemical sensing (25). Dependent on the semiconductor bandgap, the other spectral shifts (e.g., near-IR to blue upconversion) can be realized by applying similar device integration schemes with suitable semiconductor emitting devices (*SI Appendix*, Figs. S8 and S9). Current and voltage characteristics are measured from the GaInP red LED and the GaAs DJPD under different illumination powers (Fig. 1*G*). The results indicate that both the LED and the DJPD work under their optimal operating voltages (1.6–1.8 V) across a wide range of excitation powers. Large arrays of such upconversion devices (>100 × 100 devices) are formed with high fabrication yields (>99%) on a 2-inch GaAs

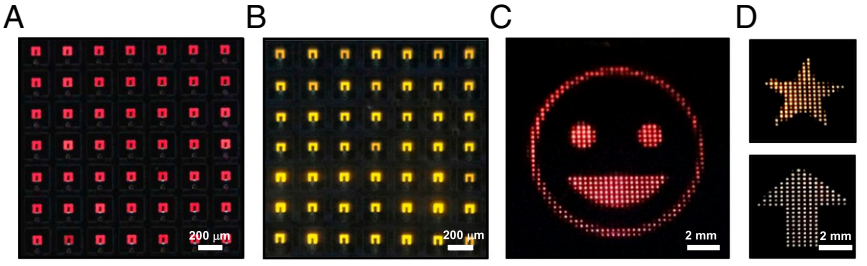

Fig. 2. Optical images of microscale IR-to-visible upconversion device arrays. (*A* and *B*) Optical image of fabricated IR-to-red (*A*) and IR-to-yellow (*B*) upconversion device arrays under 810-nm IR illumination. (*C* and *D*) Photographs of representative images captured with a red (*C*) emission upconversion device array and a yellow (*D*) emission upconversion device array under patterned IR illuminations.

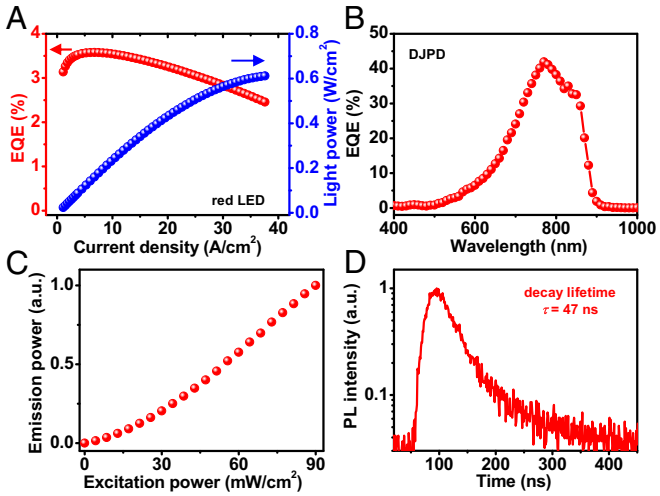

Fig. 3. Measured performance of the IR-to-red upconversion device. (*A*) EQE (red curve) and light output power density (blue curve) as a function of current density for the GaInP red LED. (*B*) EQE spectrum of the GaAs DJPD. (*C*) Emission power as a function of the excitation light (at 810 nm) density for the integrated upconversion device. (*D*) Photoluminescence decay of the integrated upconversion device. PL, photoluminescence.

substrate. Representative photographs of IR-to-red and IR-to-yellow upconversion device arrays are shown in Fig. 2 *A* and *B*, respectively. Fig. 2 *C* and *D* (with more examples in *SI Appendix*, Fig. S10) presents multiple captured red-emitting and yellow-emitting images by passing collimated light from an 810-nm LED through different patterned transparency masks, demonstrating direct IR-to-visible imaging capabilities.

Performance of Upconversion Devices. Fig. 3 further characterizes the detailed performance measured from our designed upconversion device structures. Independent thin-film GaInP red LED and GaAs DJPD (with details provided in *SI Appendix*, Tables S2 and S3) devices with the same designs as those in the integrated heterostructure (Fig. 1*B* and *SI Appendix*, Table S1) are fabricated separately on GaAs substrates and released onto polyimide substrates by transfer printing (26, 27). Fig. 3*A* plots the measured external quantum efficiency (EQE) and output light power vs. current density for a GaInP red LED with a size of 80 × 80 μm^2. The EQE peaks at 3.6% under an input current density of ∼5 A/cm^2 and decreases at higher currents, probably as a result of heating. The EQE of GaInP LEDs is mainly limited by the inefficient light extraction associated with high refractive indices (n = 3.5) of III–V materials, with an estimated extraction efficiency of $1/2n^2$ = 3.9% (28). The fact that the calculated extraction efficiency is very close to the experimental EQE suggests that the epi-grown GaInP LED has a near-unity (>90%) internal quantum yield. The AlGaInP yellow LEDs with similar structures present relatively lower EQE than the red ones due to the increased Al composition in the active emitting layers (29). Fig. 3*B* shows the measured EQE spectra for the GaAs DJPD under normal incidence, while EQE spectra of the two separate subcells are provided in *SI Appendix*, Fig. S6. The GaAs DJPD exhibits a wide excitation range from 600 to 900 nm, with a maximum EQE reaching 42% at ∼770 nm, where the top and bottom GaAs cells are current matched. The deviation from the theoretical limit (50% for the two-photon process) is mainly associated with the reflection loss at the nonoptimized III–V/air interface. With the growth substrate removed, photon response by backside illumination is also observed (*SI Appendix*, Fig. S6). The excitation spectra in our upconversion devices can be tuned by selecting appropriate semiconductors. Combining the red LED and the DJPD, the fabricated upconversion device reaches a practical IR-to-visible conversion efficiency of 1.5% under normal incidence. Separately measured results for the red LED and DJPD indicate that very high (>90%) internal electron–photon conversion efficiencies are realized for these high-quality III–V-based devices, and the external quantum efficiencies are mostly limited by the nonideal optical absorption and extraction. Implemented with optimal optical designs for the LED and the DJPD (30–32), the upconversion efficiency of the integrated device can be further improved and approach the thermodynamic limit (50% for the two-photon process) without theoretical constraints (*SI Appendix* and *SI Appendix*, Figs. S1 and S2).

The fully formed IR-to-red upconversion device is excited by an incoherent, low-power IR LED bulb (∼810 nm), with its emission spectra captured by a fiber-coupled spectrometer. The integrated emission intensity (from 610 to 650 nm) vs. incident IR power density is plotted in Fig. 3*C*. We can clearly see that the emission is linearly dependent on the excitation incidence at a power as low as 10 mW/cm^2, in comparison with one-sun illumination (100 mW/cm^2). This is because both high-performance LEDs and detectors can operate linearly under low-injection currents or illumination. At lower excitation power (<10 mW/cm^2), the sublinear behavior is mainly attributed to the low LED efficiency associated with nonradiative recombination at low currents. By contrast, upconversion processes based on traditional nonlinear energy transfer mechanisms exhibit much lower efficiencies (∼0.01%) at such low-incident powers and require much higher irradiance (typically >1 W/cm^2) to reach linear operation and saturated efficiencies (∼2%) (4, 33). The impulse response of

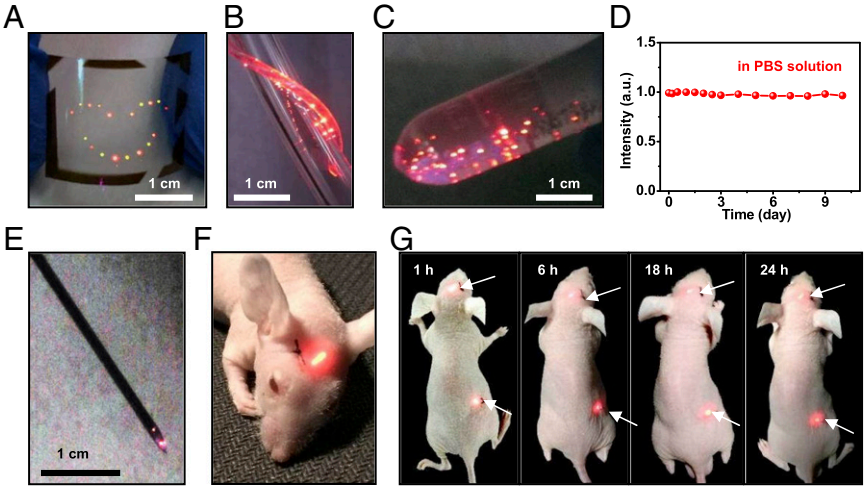

Fig. 4. Released thin-film microscale upconversion devices integrated with various systems. (*A*) An array of devices transferred onto a flexible PET film under uniform IR illumination. (*B*) A collection of devices integrated with a stretchable PDMS fiber with guided IR light, wrapped onto a plastic cylindrical tube. (*C*) A collection of released devices dispersed in PBS. (*D*) The luminance stability of encapsulated devices for different immersion times in PBS. (*E*) Microscale devices injected from a syringe needle. (*F*) Image of a nude mouse with devices implanted s.c. (*G*) Photos showing the luminance stability of the implanted devices within 24 h. PDMS, polydimethylsiloxane; PET, polyethylene terephthalate.

the upconverted photoluminescence following a 30-ns excitation pulse (780-nm laser) is shown in Fig. 3*D* and *SI Appendix*, Fig. S14. Measured elapsed time for the increase in the upconversion luminescence in response to the excitation pulse is ∼10 ns, and the initial decay exhibits an exponential lifetime of 47 ns, which is due primarily to the resistive-capacitive time constant of the circuit. These results indicate that our upconversion devices show a fast response superior to previously reported materials and devices (7, 13, 21). To summarize, the fabricated microscale device presents highly efficient IR-to-visible upconversion with broadband sensitivity, linear responsivity, and fast response (*SI Appendix*, Table S5).

Freestanding Upconversion Devices on Heterogeneous Substrates. The microscale, thin-film upconversion devices are released from the GaAs growth substrate by selectively removing the $Al_{0.95}Ga_{0.05}As$ sacrificial layer in hydrofluoric acids (34). The resulted free-standing devices (∼9-μm thick) can be deterministically integrated with various heterogeneous substrates via transfer printing (34, 35). Fig. 4 *A* and *B*, respectively, illustrates arrays of microscale devices on flexible polyethylene terephthalate and stretchable polydimethylsiloxane substrates, with more examples included in *SI Appendix*, Figs. S11 and S12. These passive, remotely IR-powered, visible-emitting devices are operated without external power sources or interconnect circuits; thus, denser and larger device arrays can be easily obtained at high yields. Behaving like microparticles, the fully released and encapsulated upconversion devices can be suspended in solutions, transported in microfluidic tubes, and ejected via syringe needles (Fig. 4 *C* and *E*, *SI Appendix*, and Movies S1 and S2). After encapsulation, a large collection of such thin-film devices are dispersed in aqueous solutions and retain their upconversion functionality for >10 d without degradation (Fig. 4 *C* and *D*).

Biocompatibility Evaluation. Further in vitro and in vivo experiments were conducted to demonstrate potential uses of these upconversion devices in biology. Microscale devices were implanted into different subdermal regions of mice and rats (*SI Appendix*, Figs. S15–S18) with the approval of the Animal Care and Use Committee of Tsinghua University and the National Institute of Biological Sciences, Beijing. External IR light sources (810 nm) were remotely delivered into the subdermal tissue (in the head and the upper back), driving the devices to emit red light (630 nm) in freely behaving animals (Fig. 4 *F* and *G*, *SI Appendix*, Fig. S17, and Movie S3). Such IR-to-red upconversion is important for efficient visible-light delivery in biological systems, since many substances in the tissue exhibit significant absorption in the visible range. For example, the extinction coefficient of hemoglobin at 630 nm is almost one order of magnitude larger than that at 810 nm (16). To assess the in vivo biocompatibility of the encapsulated upconversion devices, histological examinations of biopsied tissue samples around the implants as well as hematological evaluations of the Sprague–Dawley rats and C57 black 6 (C57BL/6N) mice were made. After 1–3 wk of implantation, no significant inflammatory reactions were observed (*SI Appendix*, Figs. S15, S16, and S18) and the implanted devices retained their upconversion capabilities for up to 3 wk (*SI Appendix*, Figs. S15 and S17). From the representative views of H&E staining of the skin section adjacent to the devices at 1–3 wk after implantation (*SI Appendix*, Figs. S15 and S18), the eosinophilic infiltration was graded as minimal according to the number and distribution of eosinophils within the tissues surrounding the implants (36). In all, these results demonstrate the biocompatibility of the encapsulated upconversion devices as well as their chronic operation stability in biological systems.

In Vitro and In Vivo Neural Signal Interrogation. These self-powered, miniaturized IR-to-visible upconversion light sources provide unique opportunities for optogenetic stimulations by combining with genetically encoded optical actuators (37). Unlike other light delivery tools based on fiber-tethered light sources or wirelessly controlled LEDs driven by inductive coils, photovoltaic cells, or batteries (38–40), micro- and nanoscale upconverting materials and systems allows for minimally invasive s.c. implantation with visible light output by remotely delivered IR power. Despite successful demonstrations of optogenetic neuromodulation, conventional rare-earth–based upconverting materials (41–43) suffer from required high-power IR illumination (>1 W/mm^2) and slow responses. Our ultracompact (volume, $\sim 3 \times 10^{-4}$ mm^3; weight, ∼1 μg) upconversion device overcomes the challenges of the above approaches with stable, efficient, and fast IR-to-visible upconversion.

The feasibility of this concept was first explored via in vitro experiments as shown in Fig. 5. While opsins sensitive to blue and green light are commonly utilized for optogenetics, red-shifted opsins sensitive to amber and red light are also of particular interest for independent control of distinct neuron populations (44). Here, microscale upconversion devices were placed underneath cultured brain slices (∼200-μm thick) with neural cells expressing ChrimsonR (produced by Shanghai Taitool Bioscience, Co. Ltd) and illuminated with a near-IR laser (810 nm) (Fig. 5*A*). IR illumination penetrates into the brain tissue and excites red emission (630 nm) that interrogates ChrimsonR-expressing neurons, with intracellular signals recorded by a perforated whole-cell patch-clamp setup (Fig. 5*B*). Under IR illumination (810 nm) with an OD of 15 mW/mm^2, the power density of upconverted red emission (630 nm) on the device surface is estimated to be ∼1.1 mW/mm^2 (see *Methods*), above the threshold (∼1 mW/mm^2) to activate ChrimsonR (44). Photocurrents of a patch-clamped cell above the red-emitting device were recorded under pulsed illumination (duration of 10 ms, 810 nm) with various frequencies (10, 20, and 50 Hz), and the corresponding continuous bursts of spiking response are shown in Fig. 5*C*. In addition, cells responses were examined without the upconversion device underneath, suggesting that direct IR illumination cannot activate ChrimsonR-expressing neurons, which is consistent with the literature (44).

To further demonstrate the in vivo applicability, the synchronization of neural activities with upconversion devices was examined in the optogenetics experiment. IR-to-red upconversion devices were transferred onto polyimide-based flexible probe substrates and implanted into the mouse brain (*SI Appendix*, Fig. S19). As excitatory neurons in the primary somatosensory cortex

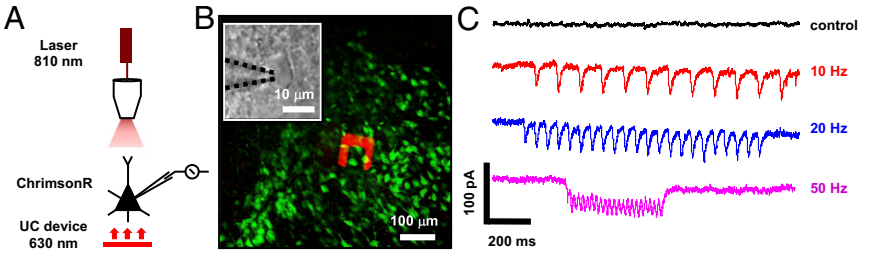

Fig. 5. In vitro optogenetic neural modulation using a microscale upconversion device. (*A*) Schematic illustration of the setup to measure intracellular signals of ChrimsonR-expressing nerves under IR illumination. (*B*) Confocal fluorescence image of an upconversion device (red color) underneath cultured neural cells expressing ChrimsonR-EGFP (green color). The *Inset* shows a whole-cell patch-clamp pipette (black dashed lines) that records photocurrent signals from a neuron. (*C*) A series of photocurrent signals recorded from a ChrimsonR-expressing neuron under IR illumination (810-nm laser) with a train of pulses (10-ms duration) at 10, 20, and 50 Hz (with the upconversion device at the *Bottom*), as well as the control results (without the upconversion device). UC, upconversion.

(S1) show strong synchronization under light activation with low frequencies (45), the local field potential (LFP) can be measured in the S1 to analyze synchronous local network activities. To specifically label excitatory neurons in the S1, ChrimsonR is expressed in the S1 of calcium/calmodulin dependent protein kinase II alpha (Camk2a)-Cre knock-in mice (Fig. 6 *A* and *B*). To evaluate the caused injury or neuroinflammatory response of implantation, the astrocyte activation and microglia accumulation in the S1 were estimated within various times (Fig. 6*C* and *SI Appendix*, Fig. S20). The implanted region exhibited normal immunological effects, and immunoreactive glial responses were similar to those results based on optical fiber probes, flexible devices and fluorescent nanoparticles (38–41). In this invasive operation, the tissue lesion was mainly attributed to the probe substrate and encapsulation layers, and it could be further minimized using cellular-scale device structures (*SI Appendix*, Fig. S21) and other advanced thin-film coating techniques (46). In vivo recordings of LFP in the S1 were performed under transcranial IR irradiation (810 nm) in conscious Camk2a-Cre mice, where the upconversion device probe is facing the ChrimsonR-expressing region and under IR illumination (*SI Appendix*, Fig. S19). Pulsed stimulation at 8 Hz with upconverted light (630 nm) induced an increased LFP power at the same frequency (Fig. 6 *D–F*), indicating that such periodic optical activations generate theta oscillations in the cortical region (45). Control groups without ChrimsonR expression, absence of upconversion devices probe, or only IR light were performed and all showed no significant LFP power increase (Fig. 6 *D–F*), suggesting the upconversion devices could effectively emit red light to manipulate the activated ChrimsonR-expressing neurons. Taken together, these results establish the utility of our microscale upconversion devices as implantable light sources for wireless optogenetic control of in vitro and in vivo neuroactivities.

Discussion

In conclusion, concepts presented here demonstrate materials and device strategies for highly efficient IR-to-visible upconversion that bypass many limitations of previously explored

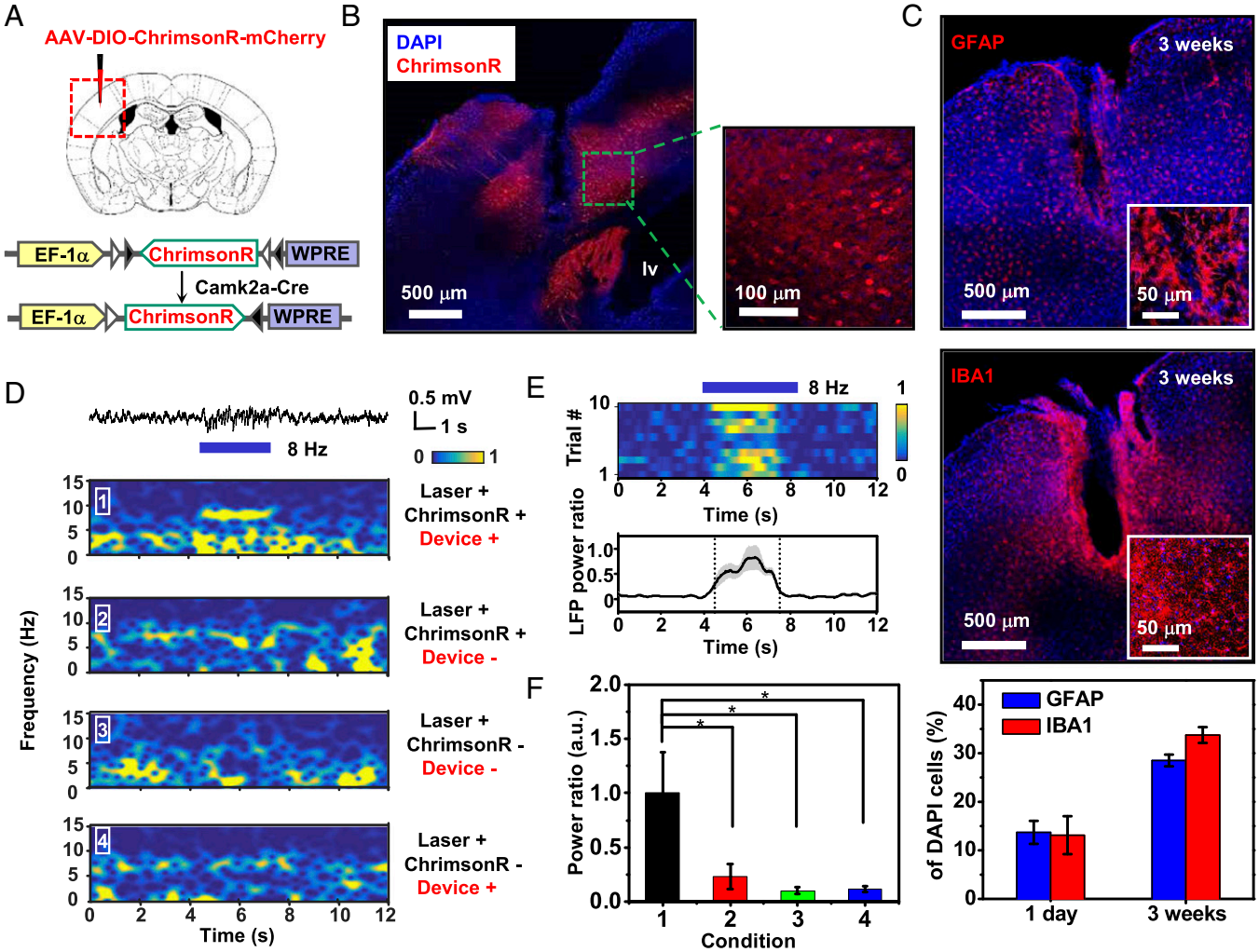

Fig. 6. In vivo optogenetic stimulation with upconversion devices. (*A*) The strategy of labeling of Camk2a neurons with ChrimsonR by injecting AAV-DIO-ChrimsonR–mCherry-WPRE vectors into the primary somatosensory cortex (S1) of Camk2a-Cre mice. (*B*) Images of ChrimsonR-mCherry (red) expression in S1. (*C*) Images of S1 regions after 3 wk of implantation, respectively stained for GFAP+ astrocytes (*Top*) or IBA1+ microglia (*Middle*), and percentages of the cell population indicated by DAPI cells (*Bottom*) ($n = 3$ mice for each group). (*D*) LFP recording in response to 8-Hz IR stimulation (810 nm, 10-ms pulses, 3-s duration) of S1 under different conditions. (*E*) The effects of IR stimulation. (*Top*) Heatmaps draw power at 8 Hz of individual trials. (*Bottom*) Average of normalized power at 8 Hz. (*F*) Normalized power ratio of the light activation under the corresponding conditions of *D* ($n = 3$ mice, 10 trials per mouse). *$P <$ 0.05, *t* test. AAV, adeno-associated virus; DIO, double-floxed inverted open reading frame; IBA1, ionized calcium-binding adapter molecule 1; WPRE, woodchuck hepatitis virus posttranscriptional regulatory element.

techniques. Considering that epi-grown inorganic semiconductor devices (LEDs, solar cells, etc.) have already realized very high internal energy conversion efficiencies (30, 32), it was observed that the upconversion efficiency of our current device design is mainly constrained by the low LED extraction efficiency. Advanced surface treatments and optical coatings, such as textures and photonic crystals (31, 35, 47), can immediately lead to higher upconversion efficiencies. In addition, it will be highly desirable to further scale down the device geometry to cellular scale (<10 μm) and even molecular scale (<100 nm), and advanced bottom-up and top-down fabrication approaches (48, 49) can be utilized to achieve device structures with much smaller footprints. Such micro- and nanostructured geometries are not only advantageous for improved biointegration but also can significantly mitigate the light confinement by approaching the subwavelength scales (50), ultimately reaching thermodynamic limits (*SI Appendix*). Some preliminary explorations were performed to achieve a device structure with a dimension of <10 μm, similar to the size of neurons (*SI Appendix*, Fig. S21).

The involvement of other semiconductors, like gallium nitrides, silicon, and indium arsenide, could be used to explore excitation and emission at other wavelengths, enabling versatile sensing and displaying capabilities. Besides direct epi-growth, approaches like wafer bonding and transfer printing can be explored to realize highly compact, heterogeneously integrated structures. In particular, it would be highly desirable to develop devices upconverting IR to blue and green colors (with preliminary work shown in *SI Appendix*, Fig. S9). By combining with light-sensitive receptors or drugs (51), these miniaturized devices can be applied to deep-tissue light stimulation or therapy. These results provide routes for high-performance upconversion materials and devices and their unprecedented potential as optical biointerfaces.

ACKNOWLEDGMENTS. We thank C. Z. Ning, Y. Huang, Y. Luo, and Z. Hao (Tsinghua University) for their help in experiments and valuable discussions. The research is supported by National Natural Science Foundation of China Grants 51602172 (to X.S.) and 51601103 (to L.Y.) and 1000 Youth Talents Program in China (to L.Y. and X.S.).

1. Raman CV (1928) A new radiation. *Indian J Phys* 2:387–398.
2. Auzel F (2004) Upconversion and anti-stokes processes with f and d ions in solids. *Chem Rev* 104:139–173.
3. Zhou B, Shi B, Jin D, Liu X (2015) Controlling upconversion nanocrystals for emerging applications. *Nat Nanotechnol* 10:924–936.
4. Zhang F (2015) *Photon Upconversion Nanomaterials* (Springer, Berlin).
5. Wang F, et al. (2011) Tuning upconversion through energy migration in core-shell nanoparticles. *Nat Mater* 10:968–973.
6. Lay A, et al. (2017) Upconverting nanoparticles as optical sensors of nano- to micro-Newton forces. *Nano Lett* 17:4172–4177.
7. Liu Y, et al. (2017) Amplified stimulated emission in upconversion nanoparticles for super-resolution nanoscopy. *Nature* 543:229–233.
8. Trupke T, Shalav A, Richards BS, Wurfel P, Green MA (2006) Efficiency enhancement of solar cells by luminescent up-conversion of sunlight. *Sol Energy Mater Sol Cells* 90: 3327–3338.
9. Zou WQ, Visser C, Maduro JA, Pshenichnikov MS, Hummelen JC (2012) Broadband dye-sensitized upconversion of near-infrared light. *Nat Photonics* 6:560–564.
10. Briggs JA, Atre AC, Dionne JA (2013) Narrow-bandwidth solar upconversion: Case studies of existing systems and generalized fundamental limits. *J Appl Phys* 113: 124509.
11. Green MA, Bremner SP (2016) Energy conversion approaches and materials for high-efficiency photovoltaics. *Nat Mater* 16:23–34.
12. Yang Y, Zhang YH, Shen WZ, Liu HC (2011) Semiconductor infrared up-conversion devices. *Prog Quant Electron* 35:77–108.
13. Yu H, et al. (2016) High-gain infrared-to-visible upconversion light-emitting phototransistors. *Nat Photon* 10:129–134.
14. Downing E, Hesselink L, Ralston J, Macfarlane R (1996) A three-color, solid-state, three-dimensional display. *Science* 273:1185–1189.
15. Ha S-T, Shen C, Zhang J, Xiong Q (2016) Laser cooling of organic–inorganic lead halide perovskites. *Nat Photon* 10:115–121.
16. Weissleder R (2001) A clearer vision for in vivo imaging. *Nat Biotechnol* 19:316–317.
17. Idris NM, et al. (2012) In vivo photodynamic therapy using upconversion nanoparticles as remote-controlled nanotransducers. *Nat Med* 18:1580–1585.
18. Mura S, Nicolas J, Couvreur P (2013) Stimuli-responsive nanocarriers for drug delivery. *Nat Mater* 12:991–1003.
19. Yang D, et al. (2015) Current advances in lanthanide ion (Ln(3+))-based upconversion nanomaterials for drug delivery. *Chem Soc Rev* 44:1416–1448.
20. Aouani H, Rahmani M, Navarro-Cía M, Maier SA (2014) Third-harmonic-upconversion enhancement from a single semiconductor nanoparticle coupled to a plasmonic antenna. *Nat Nanotechnol* 9:290–294.
21. Wang J, et al. (2014) Enhancing multiphoton upconversion through energy clustering at sublattice level. *Nat Mater* 13:157–162.
22. Ye C, Zhou L, Wang X, Liang Z (2016) Photon upconversion: From two-photon absorption (TPA) to triplet-triplet annihilation (TTA). *Phys Chem Chem Phys* 18: 10818–10835.
23. Wu MF, et al. (2016) Solid-state infrared-to-visible upconversion sensitized by colloidal nanocrystals. *Nat Photon* 10:31–34.
24. Zhao L, Thompson P, Faleev N, Prather D, Appelbaum I (2007) Two-photon passive electro-optic upconversion in a GaAs/AlGaAs heterostructure device. *Appl Phys Lett* 90:121132.
25. Wong HT, Chan HL, Hao J (2010) Towards pure near-infrared to near-infrared upconversion of multifunctional GdF(3):Yb(3+),Tm(3+) nanoparticles. *Opt Express* 18: 6123–6130.
26. Meitl MA, et al. (2006) Transfer printing by kinetic control of adhesion to an elastomeric stamp. *Nat Mater* 5:33–38.
27. Park SI, et al. (2009) Printed assemblies of inorganic light-emitting diodes for deformable and semitransparent displays. *Science* 325:977–981.
28. Schubert EF (2006) *Light-Emitting Diodes* (Cambridge Univ Press, New York).
29. Lee JW, et al. (2016) An elegant route to overcome fundamentally-limited light extraction in AlGaN deep-ultraviolet light-emitting diodes: Preferential outcoupling of strong in-plane emission. *Sci Rep* 6:22537.
30. Schnitzer I, Yablonovitch E, Caneau C, Gmitter TJ (1993) Ultrahigh spontaneous emission quantum efficiency, 99.7-percent internally and 72-percent externally, from AlGaAs/GaAs/AlGaAs double heterostructures. *Appl Phys Lett* 62:131–133.
31. Wierer JJ, David A, Megens MM (2009) III-nitride photonic-crystal light-emitting diodes with high extraction efficiency. *Nat Photon* 3:163–169.
32. Green MA, et al. (2017) Solar cell efficiency tables (version 50). *Prog Photovolt Res Appl* 25:668–676.
33. Page RH, et al. (1998) Upconversion-pumped luminescence efficiency of rare-earth-doped hosts sensitized with trivalent ytterbium. *J Opt Soc Am B* 15:996–1008.
34. Yoon J, et al. (2010) GaAs photovoltaics and optoelectronics using releasable multilayer epitaxial assemblies. *Nature* 465:329–333.
35. Sheng X, et al. (2014) Printing-based assembly of quadruple-junction four-terminal microscale solar cells and their use in high-efficiency modules. *Nat Mater* 13:593–598.
36. Macleod TM, Williams G, Sanders R, Green CJ (2005) Histological evaluation of Permacol as a subcutaneous implant over a 20-week period in the rat model. *Br J Plast Surg* 58:518–532.
37. Deisseroth K (2011) Optogenetics. *Nat Methods* 8:26–29.
38. Kim TI, et al. (2013) Injectable, cellular-scale optoelectronics with applications for wireless optogenetics. *Science* 340:211–216.
39. Park SI, et al. (2015) Soft, stretchable, fully implantable miniaturized optoelectronic systems for wireless optogenetics. *Nat Biotechnol* 33:1280–1286.
40. Park SI, et al. (2015) Ultraminiaturized photovoltaic and radio frequency powered optoelectronic systems for wireless optogenetics. *J Neural Eng* 12:056002–56002.
41. Chen S, et al. (2018) Near-infrared deep brain stimulation via upconversion nanoparticle-mediated optogenetics. *Science* 359:679–684.
42. Hososhima S, et al. (2015) Near-infrared (NIR) up-conversion optogenetics. *Sci Rep* 5: 16533.
43. Huang K, Dou QQ, Loh XJ (2016) Nanomaterial mediated optogenetics: Opportunities and challenges. *RSC Adv* 6:60896–60906.
44. Klapoetke NC, et al. (2014) Independent optical excitation of distinct neural populations. *Nat Methods* 11:338–346.
45. Cardin JA, et al. (2009) Driving fast-spiking cells induces gamma rhythm and controls sensory responses. *Nature* 459:663–667.
46. Fang H, et al. (2016) Ultrathin, transferred layers of thermally grown silicon dioxide as biofluid barriers for biointegrated flexible electronic systems. *Proc Natl Acad Sci USA* 113:11682–11687.
47. Sheng X, et al. (2011) Design and fabrication of high-index-contrast self-assembled texture for light extraction enhancement in LEDs. *Opt Express* 19:A701–A709.
48. Huang Y, Duan X, Lieber CM (2005) Nanowires for integrated multicolor nanophotonics. *Small* 1:142–147.
49. Hobbs RG, Petkov N, Holmes JD (2012) Semiconductor nanowire fabrication by bottom-up and top-down paradigms. *Chem Mater* 24:1975–1991.
50. Yan RX, Gargas D, Yang PD (2009) Nanowire photonics. *Nat Photon* 3:569–576.
51. Yun SH, Kwok SJJ (2017) Light in diagnosis, therapy and surgery. *Nat Biomed Eng* 1:0008 (2017).

Supporting Information for

Microscale Optoelectronic Infrared-to-Visible Upconversion Devices and Their Use as Injectable Light Sources

He Ding,[1] Lihui Lu,[2] Zhao Shi,[1] Dan Wang,[3] Lizhu Li,[1] Xichen Li,[4] Yuqi Ren,[2] Changbo Liu,[1] Dali Cheng,[1] Hoyeon Kim,[5] Noel C. Giebink,[5] Xiaohui Wang,[6] Lan Yin,[3] Lingyun Zhao,[3] Minmin Luo,[2, 7] Xing Sheng[1, *]

*Correspondence to: xingsheng@tsinghua.edu.cn

Materials and Methods

Figures S1-S21

Tables S1-S5

Movies S1-S3

References (1-8)

Materials and Methods

Theoretical analysis

Based on the detailed balance theory[1,2], the current density of a diode (either a photovoltaic detector PD or an LED) is the difference between generated carriers and recombined carriers:

$$\begin{aligned} J &= J_{generation} + J_{recombination} \\ &= J_{ph} + J_{th} - J_{rad} - J_{non-rad} \\ &= J_{ph} + J_{th} - J_{rad} / \eta_{ext} \\ &= \eta_{abs} J_{inc} + J_{th} - J_{rad} / \eta_{ext} \end{aligned}$$

J_{ph} absorbed incident photons

J_{inc} total incident photons

η_{abs} absorption efficiency

J_{th} absorbed thermal radiation from environment

$$J_{th} = \frac{2\pi(n^2+1)qkT}{h^3c^2} E_g^2 \exp\left(-\frac{E_g}{kT}\right)$$

J_{rad} radiative current

$$J_{rad} = \frac{2\pi(n^2+1)qkT}{h^3c^2} E_g^2 \exp\left(\frac{qV-E_g}{kT}\right)$$

$J_{non-rad}$ non-radiative current, include SRH recombination, Auger recombination, etc

$\eta_{ext} = \frac{J_{rad}}{J_{rad} + J_{non-rad}}$ external radiation efficiency

In the upconversion system shown in Fig. S1a, multiple (number: *m*) PDs are connected in series to supply power to an LED. Under illumination, current and voltage should satisfy (if we assume each PD has the same surface area as the LED):

$$\begin{cases} J_{LED} = J_{PD} \\ V_{LED} = mV_{PD} \end{cases}$$

By solving the above equations, we will obtain J_{LED}, J_{PD}, V_{LED} and V_{PD}. The intensity of the LED light emission should be related to the LED radiative current:

$$J_{rad-LED} = \frac{2\pi(n^2+1)qkT}{h^3c^2} E_{g-LED}^2 \exp\left(\frac{qV_{LED} - E_{g-LED}}{kT}\right)$$

The quantum yield of such an upconversion system will be:

$$QY = \frac{J_{rad-LED}}{mJ_{inc}}$$

We first assume the refractive indices of our semiconductor materials are n = 3.5, the InGaP red LED has $E_{g\text{-}LED}$ = 2.0 eV (emitting at λ = 630 nm) and η_{ext} = 100%, the GaAs PD has $E_{g\text{-}PD}$ = 1.4 eV and η_{abs} = 100% at incident wavelength λ = 808 nm (energy 1.56 eV), and the system is operated at room temperature (T = 300 K). In this case, at least 2 serially connected GaAs PDs (m = 2) are needed to provide sufficient voltage to upconvert infrared light (λ = 808 nm) to visible (λ = 630 nm). Figure S1b plots the current-voltage characteristics of the InGaP LED and the GaAs PD array (with 2 cells connected in serial) under different illumination intensities (with equivalent photon flux J_{inc} = 200, 400, 600, 800 and 1000 A/m^2, respectively). Under these ideal conditions, the system quantum yields are calculated to be nearly 50%, approaching the thermodynamic efficiency limit of two photon upconversion process.

Secondly, we vary the bandgap of the PDs in the system above. Figure S1C plots the current-voltage characteristics of the InGaP LED and the PD array (with 2 cells

connected in serial) made by semiconductors with different bandgaps ($E_{g\text{-}PD}$ = 1.0, 1.1, 1.2, 1.3 and 1.4 eV, respectively) under illumination intensity J_{inc} = 1000 A/m^2. We assume the incident photon energy is slightly larger than $E_{g\text{-}PD}$ and η_{abs} is still 100%. It can be seen that under these ideal conditions, we need $E_{g\text{-}PD}$ > 1.2 eV to approach QY = 50%. When $E_{g\text{-}PD}$ < 1.2 eV, QY decreases dramatically with $E_{g\text{-}PD}$ because the 2 serially connect PD array cannot provide sufficient voltage to turn on the red LED.

Figure S2 illustrates calculated efficiency (quantum yield) limit for our photon upconversion (and downconversion as well) systems, i.e., the upper efficiency limit of converting one or multiple photons with energy E_{ph} to one photon with an energy of 2 eV (emitting at λ = 630 nm) by using interconnected optoelectronic devices (PDs and LEDs). Figure S2a plots the ideal case at T = 0 K, and the thermodynamic limits should be:

photon energy E_{ph} (eV)	number of photons needed	quantum yield limit
$E_{ph} > 2$	1	1.0
$1 < E_{ph} < 2$	2	0.5
$2/3 < E_{ph} < 1$	3	0.33
$1/2 < E_{ph} < 2/3$	4	0.25
$2/5 < E_{ph} < 1/2$	5	0.2
…	…	…

Figure S2b plots the detailed balance limits at T = 300 K, with PD absorption efficiency η_{abs} = 100%, and LED external radiative efficiency η_{ext} = 100%. Figure S2c plots a more realistic case at T = 300 K, with PD η_{abs} = 90%, and LED η_{ext} = 50%. Since state-of-the-art PDs and LEDs have been demonstrated to have very high

internal and external quantum efficiencies [2,3], the two photon upconversion process can reach a practical quantum yield > 20% (and even approaches 50%) with realistic optoelectronic device design [1,2].

Device fabrication

The upconversion device structure is grown on a GaAs substrate by metal-organic chemical vapor deposition (MOCVD). The detailed structure is listed in Fig. S1 and Table S1, which involves (from bottom to top): the GaAs substrate, an $Al_{0.95}Ga_{0.05}As$ sacrificial layer, a GaAs double junction photodiode (DJPD), a distributed Bragg reflector (DBR) and an AlGaInP LED ($Ga_{0.5}In_{0.5}P$ for red LED or $Al_{0.15}Ga_{0.35}In_{0.5}P$ for yellow LED). In the DJPD, the two GaAs subcells are connected by a thin-film, highly doped GaAs based tunneling junction, and the thickness of each subcell is designed to realize current match and optimal efficiency at 810 nm. Independent AlGaInP LED and GaAs PD structures (parameters listed in Table S2 and S3) are also epitaxially grown and fabricated separately, which are used for optical and electrical characterization. Active areas of the GaAs PD (220×220 μm^2) and the AlGaInP LED (80×80 μm^2) are defined by photolithographic process and acid based wet etching. Sputtered metal layers (Cr/Au/Cu/Au=10/20/500/60 nm) serve as interconnect contacts. After removing the $Al_{0.95}Ga_{0.05}As$ sacrificial layer in a hydrofluoric acid (HF) based solution (HF:water = 1:10 by volume), patterned photoresist anchors tether freestanding thin-film devices on the GaAs substrates. Using poly(dimethylsiloxane) (PDMS) stamps, released devices are picked up and

transferred onto thin flexible polyimide (PI) films (or any other carrier substrates) with a spun coated adhesive layer [4]. Spun coated SU-8 and PDMS layers (~ 10 μm thick) are used for waterproof encapsulation. Independent red GaInP LED and GaAs PD cell structures (parameters listed in Table S2, S3 and S4) are also epitaxially grown and fabricated separately, which are used for optical and electrical characterization.

A detailed description of the process to fabricate the freestanding microscale upconversion devices is listed below:

Etch LED

1. Deposit 500 nm thick SiO_2 by PECVD.
2. Clean the wafer with acetone, isopropyl alcohol (IPA), deinoized (DI) water.
3. Dehydrate at 110 °C for 10 min.
4. Spin coat positive photoresist (PR) (SPR220-3.0, Microchem, 500 rpm / 5 s, 3000 rpm / 45 s) and soft-bake at 110 °C for 1.5 min.
5. Expose PR with UV lithography tools (URE-2000/25, IOE CAS) with irradiance for 300 mJ/cm^2 through a chrome mask and post-bake at 110 °C for 1.5 min.
6. Develop PR in aqueous base developer (AZ300 MIF), rinse with DI water and hard-bake at 110 °C for 20 min.
7. Etch SiO_2 with buffered oxide etchant (BOE 6:1) for ~100 s and rinse with DI water.
8. Clean the PR in processed wafer using acetone, IPA, DI water.

9. Etch GaP in a mixture of $KOH/K_3[Fe(CN)_6]/H_2O$ (1:4:15, by weight) at 80 °C (hot water bath) for 60 s with gently shaking and rinse with DI water.
10. Clean processed wafer in dilute hydrochloric acid (HCl : DI water = 1:5, by volume) for 20 sec and rinse with DI water.
11. Clean the processed wafer (acetone, IPA, DI water) and dehydrate at 110 °C for 10 min.
12. Pattern PR SPR220-3.0.
13. Etch InAlP/MQWs/InAlP/DBR in a mixture of $HCl:H_3PO_4$ (1:1, by volume) for 10 s with vigorous shaking, repeat (3~4 times) until the surface is clean and shiny, and then rinse with DI water.
14. Etch n-GaAs in a mixture of $H_3PO_4/H_2O_2/H_2O$ (3:1:25 by volume) for 5 min and rinse with DI water.
15. Remove PR (SPR220-3.0) in processed wafer using acetone, IPA, DI water.
16. Remove the SiO_2 with BOE 6:1 solution for ~2 mins and rinse with DI water.

Etch PD

17. Clean the processed wafer in step 16 (acetone, IPA, DI water) and dehydrate at 110 °C for 10 min.
18. Pattern PR SPR220-3.0.
19. Etch n+ InGaP in a mixture of HCl/H_3PO_4 (1:1, by volume) for ~20 s with vigorous shaking and rinse with DI water.

20. Etch GaAs in a mixture of $H_3PO_4/H_2O_2/H_2O$ (3:1:25, by volume) for ~13 min and rinse with DI water.
21. Etch p+ InGaP in concentrated HCl (+10% ethanol) for 10 s with vigorous shaking, repeat (2~3 times) until clean and then rinse with DI water.

Contact metallization

22. Clean the processed wafer in step 21 (acetone, IPA, DI water) and dehydrate at 110 °C for 10 min.
23. Spin-coat negative photoresist (AZ nLOF 2070, 500 rpm/ 5 s, 3000 rpm/ 45 s) and soft-bake at 110 °C for 2 min.
24. Expose with 365 nm optical lithography with irradiance for 45 mJ/cm^2 through a chrome mask and post-exposure bake at 110 °C for 35 s.
25. Develop PR in aqueous base developer (AZ300 MIF) and rinse with DI water.
26. Deposit 20/200 nm of Cr/Au by electron beam evaporation.
27. Lift-off PR in acetone.

Epoxy encapsulation

28. Clean the processed wafer in step 27 (acetone, IPA, DI water) and dehydrate at 110 °C for 10 min.
29. Expose to ultraviolet induced ozone (UV Ozone) for 10 min.
30. Spin-coat with epoxy (SU8-2002, 500 rpm/ 5 s, 3000 rpm/ 45 s).
31. Soft-bake at 65 °C for 1 min and 95 °C for 1 min.

32. Pattern epoxy by exposing with UV lithography tools with irradiance for 100 $mJ \cdot cm^{-2}$ through a chrome mask.
33. Post-bake at 65 °C for 1 min and 95 °C for 2 min.
34. Develop in propylene glycol monomethyl ether acetate (PGMEA) for 1 min and rinse with IPA.
35. Hard-bake at 110 °C for 20 min.

Interconnect metallization

36. Clean the processed wafer in step 35 (acetone, IPA, DI water) and dehydrate at 110 °C for 10 min.
37. Pattern PR AZ nLOF 2070.
38. Deposit 10/20/500/100 nm of Cr/Au/Cu/Au by sputter coater.
39. Lift-off PR in acetone.

Separation, anchoring and undercut

40. Clean the processed wafer in step 39 (acetone, IPA, DI water) and dehydrate at 110 °C for 10 min.
41. Pattern PR SPR220-3.0.
42. Etch GaAs in a mixture of $H_3PO_4/H_2O_2/H_2O$ (3:1:25, by volume) for 9 min and rinse with DI water.
43. Clean the processed wafer in step 42 (acetone, IPA, DI water).
44. Pattern PR SPR220-3.0.

45. Etch in diluted HF (49% HF : DI water = 1:10, by volume) to release the devices from growth substrates for 1.2 hour and rinse with DI water.

Transfer printing

46. Clean a glass substrate with standard RCA clean process 1 (NH_4OH : H_2O_2 : H_2O = 1:1:5, 80 °C) for 10 min.
47. Dehydrate at 110 °C for 10 min.
48. Spin-coat with poly(dimethylsiloxane) (PDMS, pre-polymer : curing agent = 10:1, by weight, 500 rpm/ 5 s, 3000 rpm/ 45 s) and soft-bake at 110 °C for 3 min.
49. Paste 50 μm thick polyimide (PI) film on the glass and post-bake at 110 °C for 10 min.
50. Clean the PI film (acetone, IPA, DI water).
51. Pattern PR AZ nLOF 2070.
52. Deposit 30 nm of Cr as the markers by electron beam evaporation.
53. Lift-off PR in acetone.
54. Clean the processed substrate in step 53 (acetone, IPA, DI water).
55. Dehydrate at 110 °C for 10 min.
56. Spin-coat with adhesive liquid (3000 rpm, 45 s) on the substrate and soft-bake at 110 °C for 5 min.
57. Transfer printing the device from the source wafer onto the processed substrate with PDMS stamp.
58. Cure under to UV for 1 h and bake at 110 °C for 1 h.

59. PR (SPR220-3.0 on the device) clean by reactive ion etching with oxygen gas (O_2, 100 sccm, 90 mTorr, 150 W) for 12 min.

Device Encapsulation

60. Clean with DI water and dehydrate at 110 °C for 10 min.
61. Expose to ultraviolet induced ozone (UVO) for 10 min.
62. Spin-coat with epoxy (500 rpm/ 5 s, 3000 rpm/ 45 s), cure under to UV for 30 min and bake at 100 °C for 30 min.
63. Spin-coat with PDMS (500 rpm/ 5s, 2000 rpm/ 45 s) and bake at 110 °C for 30 min.
64. A bilayer of PDMS by a second spin-coat process (Step 63).

Device characterization

Current–voltage characteristics are recorded using a computer-controlled Keithley 2400 source meter. The GaAs PDs are illuminated under an infrared LED bulb with a wavelength of 810 nm (ThorLabs). Electroluminescence of LEDs and photoluminescence of upconversion devices are measured with a spectrometer (HR2000+, Ocean Optics). EQE spectra of the GaAs DJPD are measured using a solar cell quantum efficiency measurement system (QEX10), in which top and bottom subcells are respectively measured with the 850 nm and 473 nm bias light saturation. EQE of the LED is measured using a spectroradiometer system with integrating sphere (LabSphere). Time-resolved photoluminenscence (PL) measurements are taken

using a streak camera (Hamamatsu C10910) with input monochomator (Princeton Instrument). A 785 nm diode laser (Coherent, OBIS LX) is focused to a spot to excite the samples and a function generator is used to modulate the laser pulse width and repetition rate to 30 ns and 1 MHz, respectively. The emission light is collected using 700 nm cutoff shortpass filter (ThorLabs). The PL lifetime results are plotted in SI Appendix, Fig. S14.

In vitro and in vivo assays

Animal care is in accordance with the institutional guidelines of Tsinghua University and National Institute of Biological Sciences in Beijing, with protocols proved by Institutional Animal Care and Use Committee (IACUC). All animals are socially housed in a 14 h/10 h (7 am – 9 pm) light/dark cycle, with food and water *ad alibitum*.

Histological examination

Encapsulated upconversion devices are implanted into subdermal regions of mice. Photographs and movies of living mice are taken under the 810 nm IR LED illumination. Following 1–3 weeks of implantation, visual examination of subcutaneous tissues around the implant of the mice or rats under inhalational anesthesia is performed. After administration of ketamine, xylazine and acepromazine, the rats undergo transcardial perfusion with PBS and then 4% paraformaldehyde. The skin tissue around the implant is cut and fixed in

formaldehyde for 2 days. After the implanted devices are removed (or kept) from the skin tissue samples, the tissues are embedded in paraffin and cut into 4 μm thick slices serially using Leica RM2016 slicer. The tissue slices adjacent to the implanted devices are stained with hematoxylin and eosin (H&E) according to standard procedures and photographed with optical microscope (Nikon, Eclipse CI) and a digital camera (Nikon, DS-U3).

Haematological assessment

The evaluations of white blood cells, red blood cells, platelets, haemoglobin, mean corpuscular volume, mean corpuscular haemoglobin, mean corpuscular haemoglobin concentration and haematocrit are carried out in 1, 2 and 3 weeks after device implantation, respectively.

Immunohistochemistry

The flexible polyimide probe with upconversion devices is implanted into the primary somatosensaory cortex (S1) of mouse. After various periods (from 1 day to 3 weeks) following the surgery, mice are transcardially perfused with 4% PFA in 0.1 M PBS. Brains are postfixed in 4% PFA and 40 μm-thick vibratome sections are prepared. After 3×5 minutes PBS rinses, the sections are blocked in PBST (PBS + 0.3% Triton X-100) with 3% bovine serum albumin for 1 hour, and respectively incubated in rabbit anti-Iba1(1:1000, Wako) and rabbit anti-GFAP antibody (1:2000, Abcam)

dissolved in PBST at 4 °C for 24 hours. After 5×5 minutes washes in PBS, the sections are incubated with Alexa 488-conjugated goat anti-rabbit antibody (1:500, Jackson ImmunoResearch) dissolved in PBST for 2 hours at room temperature followed by 3×5 minutes washes in PBS. At last, the samples are coverslipped in 50% glyceroland slides and photographed with confocal scanning microscope (DigitalEclipse A1, Nikon). The numbers of Iba1+ microglia and GFAP+ astrocytes are counted with Fiji software (https://fiji.sc/) and their percentages in cell population indicated by DAPI are calculated.

***In vitro* optogenetics evaluation**

Electrophysiological properties of the neurons in brain slices are measured with whole-cell patch-clamp recording technique [5]. The slice preparation is carried out after the viral transgene expression following the injection of AAV2/9-CAG-ChrimsonR-EGFP for two weeks. The mice are deeply anesthetized with pentobarbital (100 mg/kg i.p.) and intracardially perfused with 5 mL ice-cold oxygenated modified artificial cerebrospinal fluid (aCSF) at a rate of 2 mL/min. After perfusion with modified aCSF containing (in mM): 225 sucrose, 119 NaCl, 2.5 KCl, 0.1 $CaCl_2$, 4.9 $MgCl_2$, 1.0 NaH_2PO_4, 26.2 $NaHCO_3$, 1.25 glucose, 3 kynurenic acid, and 1 Na L-ascorbate (Sigma-Aldrich), brains are quickly removed and placed in ice-cold oxygenated aCSF containing (in mM): 110 choline chloride, 2.5 KCl, 0.5 $CaCl_2$, 7 $MgCl_2$, 1.3 NaH_2PO_4, 25 $NaHCO_3$, 20 glucose, 1.3 Na ascorbate, and 0.6 Na pyruvate. Sagittal sections (200 μm thick) are prepared using a Leica VT1200S

vibratome. The slices are incubated for 1 hour at 34 °C with aCSF saturated with 95% O_2/5% CO_2 and containing (in mM) 125 NaCl, 2.5 KCl, 2 $CaCl_2$, 1.3 $MgCl_2$, 1.3 NaH_2PO_4, 25 $NaHCO_3$, 10 glucose, 1.3 Na ascorbate, and 0.6 Na pyruvate. Illuminated under excitation of 808 nm laser (Hi-Tech optoelectronics Co., Ltd.), the recording site of the brain slice is adjusted right above the upconversion device to receive the red emission light. The internal solution within whole-cell recording pipettes (3–6 MΩ) contains (in mM): 130 K-gluconate, 10 HEPES, 0.6 EGTA, 5 KCl, 3 Na_2ATP, 0.3 Na_3GTP, 4 $MgCl_2$, and 10 Na_2-phosphocreatine (pH 7.2–7.4). Voltage-clamp recordings are performed using a MultiClamp 700B amplifier (Molecular Devices). Traces are low-pass filtered at 2.6 kHz and digitized at 10 kHz (DigiData 1440, Molecular Devices). The data are acquired and analyzed using Clampfit 10.0 software (Molecular Devices).

During this optogenetics experiment, the output power of 808 nm IR laser is P_{IR} = 1.5 W. Taking into account the surface of the light spot zone (~ 1 cm^2), the power density (*PD*) of the laser is PD_{IR} = 1.5 W/cm^2. Considering the 37% transmission of the light after the propagation in brain tissue slice (200 μm) [6], the power density (*PD*) of the IR laser on the surface of upconversion device is $PD_{IR\text{-}UC}$ = 555 mW/cm^2. Based on the measured current in the double junction photodiode (DJPD) under the corresponding power density IR laser irradiation, the generated current (*I*) is I_{DJPD} = 0.23 mA. Assuming all the generated current in the DJPD component is transferred and supplies the red LED component in the upconversion device, and the surface of the LED is

around 5×10^{-5} cm^2, the current density (J) of the LED is $J_{LED} = 4.6$ A/cm^2. Based on the function of the power density and current density for the LED shown in Fig. 3A, the power density (PD) of the LED is $PD_{LED} = 1.1$ mW/mm^2.

Stereotaxic Surgery

Adult Camk2a-Cre (Jackson Laboratory, B6.Cg-Tg(Camk2a-cre)T29-1Stl/J, Stock No: 005359) mice are anesthetized with an intraperitoneal injection of Avertin (250 mg/Kg). A small craniotomy is made and a calibrated pulled-glass pipette (Sutter Instrument) is lowered to the S1 (coordinates 1.0 mm from Lambda, 3.0 mm from the midline, and 0.7 and 0.3 mm ventral to Lambda). Virus is delivered through a small durotomy by a glass micropipette using a microsyringe pump (Nanoliter 2000 injector with the Micro4 controller, WPI). The glass micropipette is lowered to 0.7 mm below the cortical surface. A bolus of 0.4 μL of virus (AAV2/9-CAG-DIO-ChrimsonR-tdTomato) is injected into the S1 at 0.05 μL/min. The pipette is then retracted to a depth of 0.3 mm below the surface and an additional 0.4 μL virus is injected at the same rate. The pipette is held in place for 5 min after the injection before being retracted from the brain. A silver wire (127 μm diameter, A-M system) is attached to a skull-penetrating M1 screw above olfactory bulb to serve as ground reference. For head-fixed preparations, a custom-made titanium head-plate is secured to the skull with dental acrylic. Mice are allowed to recovery and AAV expression for 2 weeks.

***In vivo* local field potential (LFP) recording**

Mice are anesthetized with isoflurane and held in place with a head post cemented to the skull. LFP recordings are made with a tungsten microelectrode. Signals are digitized and recorded by a customized Open Ephys board (http://www.open-ephys.org/). LFP data are filtered through a low-pass filter (200 Hz cut-off) and sampled at 1 kHz. The upconversion devices probe is inserted into the S1 and illuminated by a pulsed (10 ms pulses at 8 Hz for 3 seconds) 810 nm laser with a power density around 0.8 W/cm^2.

All field potential spectra are computed with the 'spectrogram' Matlab function with a resolution of ΔF = 0.1 Hz and ΔT = 20 ms per second. LFP power ratio is calculated with the presence and absence of stimulated light in 8 Hz band.

References

1 Shockley, W. & Queisser, H. J. Detailed Balance Limit of Efficiency of P-N Junction Solar Cells. *J. Appl. Phys.* **32**, 510-519 (1961).

2 Henry, C. H. Limiting Efficiencies of Ideal Single and Multiple Energy-Gap Terrestrial Solar-Cells. *J. Appl. Phys.* **51**, 4494-4500 (1980).

3 Schnitzer, I., Yablonovitch, E., Caneau, C. & Gmitter, T. J. Ultrahigh Spontaneous Emission Quantum Efficiency, 99.7-Percent Internally and 72-Percent Externally, from AlGaAs/GaAs/AlGaAs Double Heterostructures. *Appl. Phys. Lett.* **62**, 131-133 (1993).

4 T. I. Kim, M. J. Kim, Y. H. Jung, H. Jang, C. Dagdeviren, H. A. Pao, S. J. Cho, A. Carlson, K. J. Yu, A. Ameen, H. J. Chung, S. H. Jin, Z. Q. Ma, J. A. Rogers, Thin Film Receiver Materials for Deterministic Assembly by Transfer Printing. *Chem. Mater.* **26**, 3502-3507 (2014).

5 J. Ren, C. Qin, F. Hu, J. Tan, L. Qiu, S. L. Zhao, G. P. Feng, M. M. Luo, Habenula "Cholinergic" Neurons Corelease Glutamate and Acetylcholine and Activate Postsynaptic Neurons via Distinct Transmission Modes. *Neuron* **69**, 445-452 (2011).

6 L. Shi, L. A. Sordillo, A. Rodriguez-Contreras, R. Alfano, Transmission in near-infrared optical windows for deep brain imaging. *J. Biophotonics* **9**, 38-43 (2016).

7 Tamura, Y. & Shibukawa, A. Optical studies of CaS: Eu, Sm infrared stimulable phosphors. *Jpn. J. Appl. Phys.* **32**, 3187 (1993).

8 Zhong, Y. T. *et al.* Elimination of Photon Quenching by a Transition Layer to Fabricate a Quenching-Shield Sandwich Structure for 800 nm Excited Upconversion Luminescence of Nd3+ Sensitized Nanoparticles. *Adv. Mater.* **26**, 2831-2837 (2014).

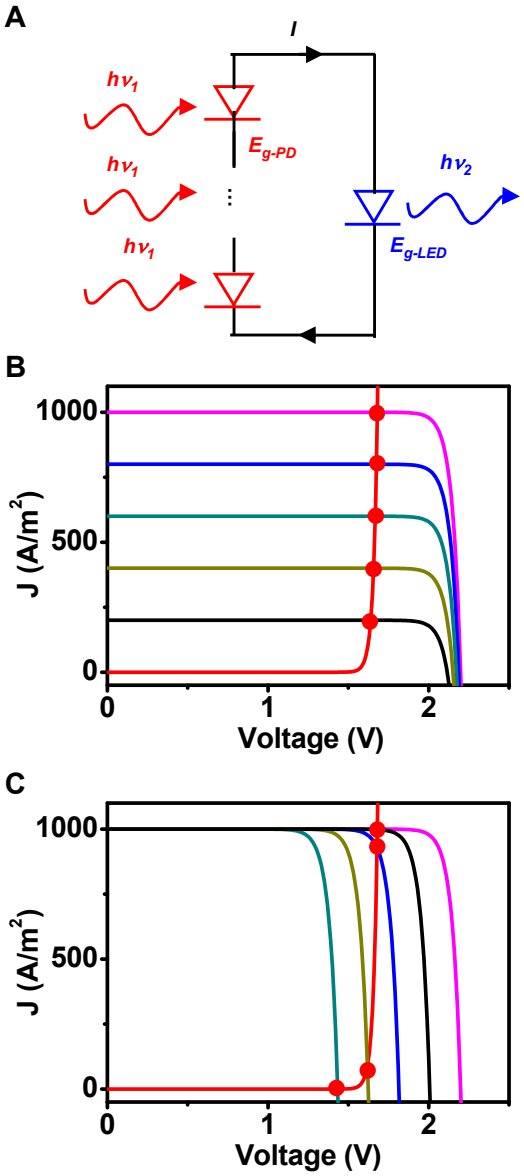

Figure S1. (**A**) Circuit diagram for our proposed upconversion design. (**B**) Calculated current density – voltage (*J–V*) characteristics of an ideal LED (bandgap 2.0 eV) and two serially connected ideal PD (bandgap 1.4 eV) under various IR illumination intensity. (**C**) Calculated *J–V* characteristics of an ideal LED (bandgap 2.0 eV) and two serially connected ideal PD with different bandgaps under IR illumination.

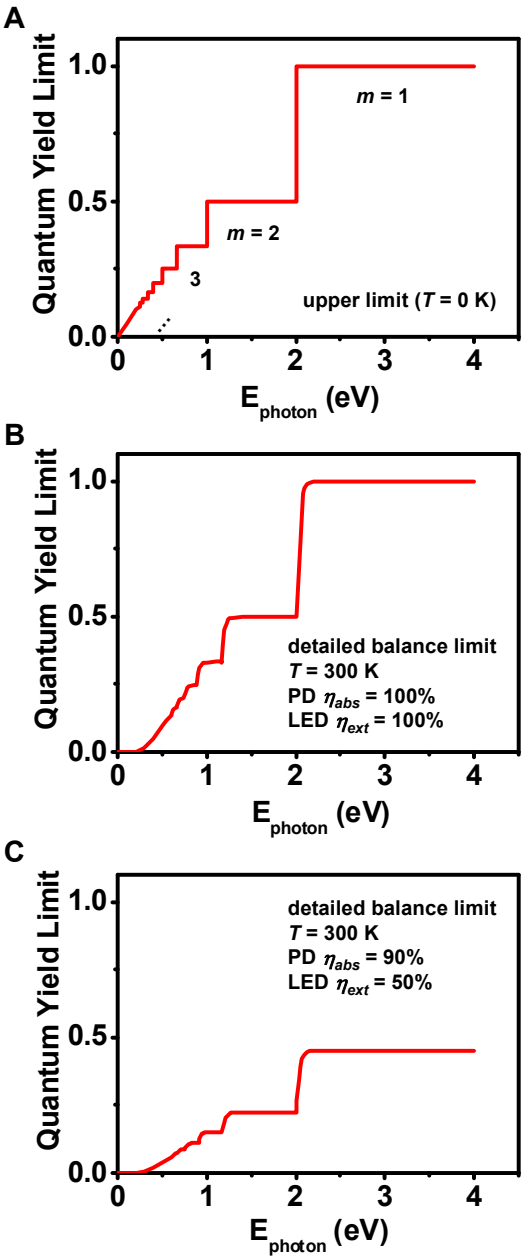

Figure S2. Calculated efficiency limits of converting one or multiple photons with energy E_{ph} to one photon with an energy of 2 eV by using interconnected PDs and LEDs, based on different assumptions.

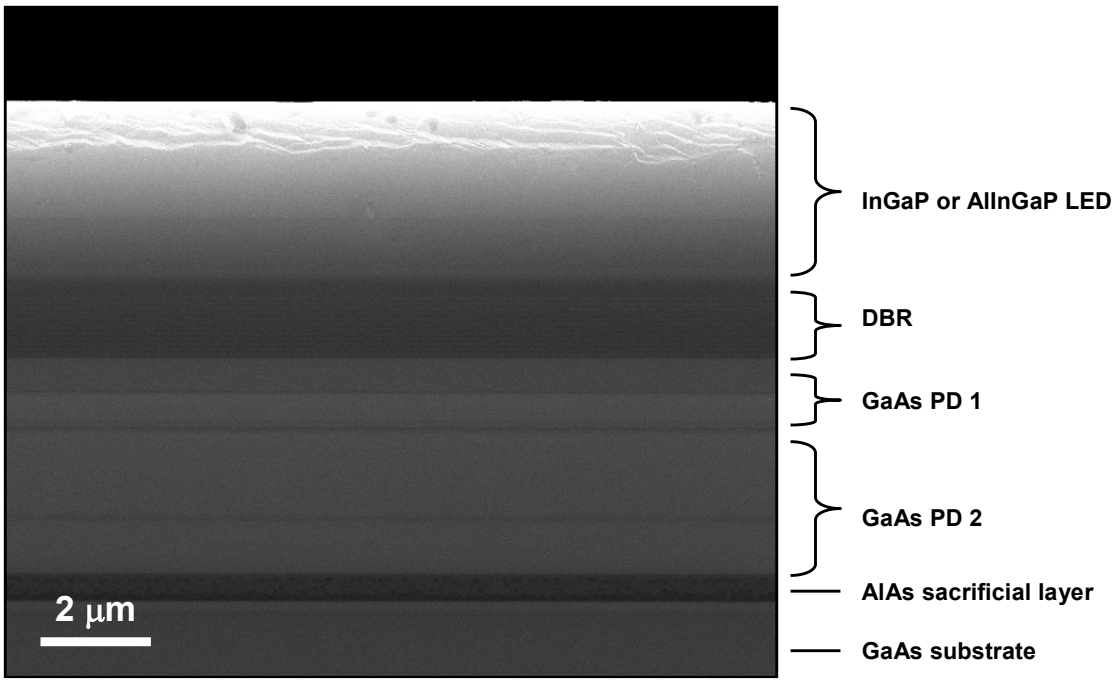

Figure S3. Cross-sectional SEM image of the multilayer stack of the upconversion device, including an InGaP red LED layer (or a similar AlInGaP yellow LED layer), a DBR layer, a GaAs DJPD layer and an $Al_{0.95}Ga_{0.05}As$ sacrificial layer on a GaAs substrate.

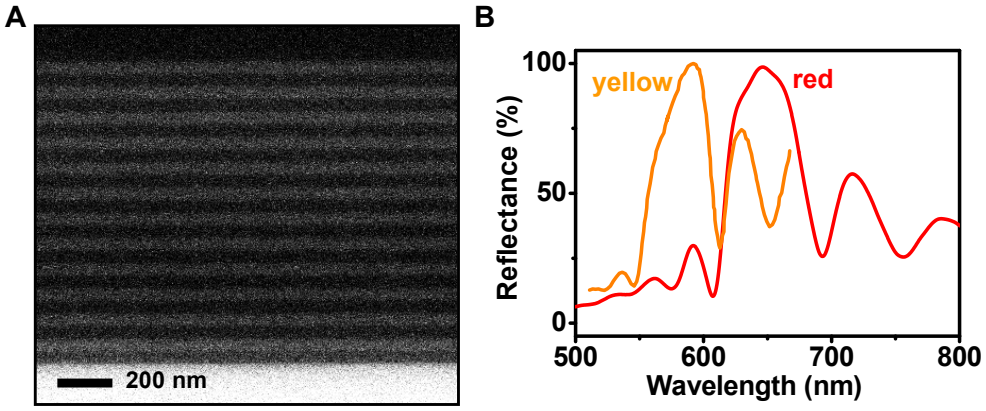

Figure S4. (**A**) Cross-sectional SEM image of the DBR layer designed below the GaInP red LED. (**B**) Measured reflectance spectra of the DBRs optimized for the GaInP red LED (peak at 630 nm) and the AlGaInP yellow LED (peak at 590 nm), respectively.

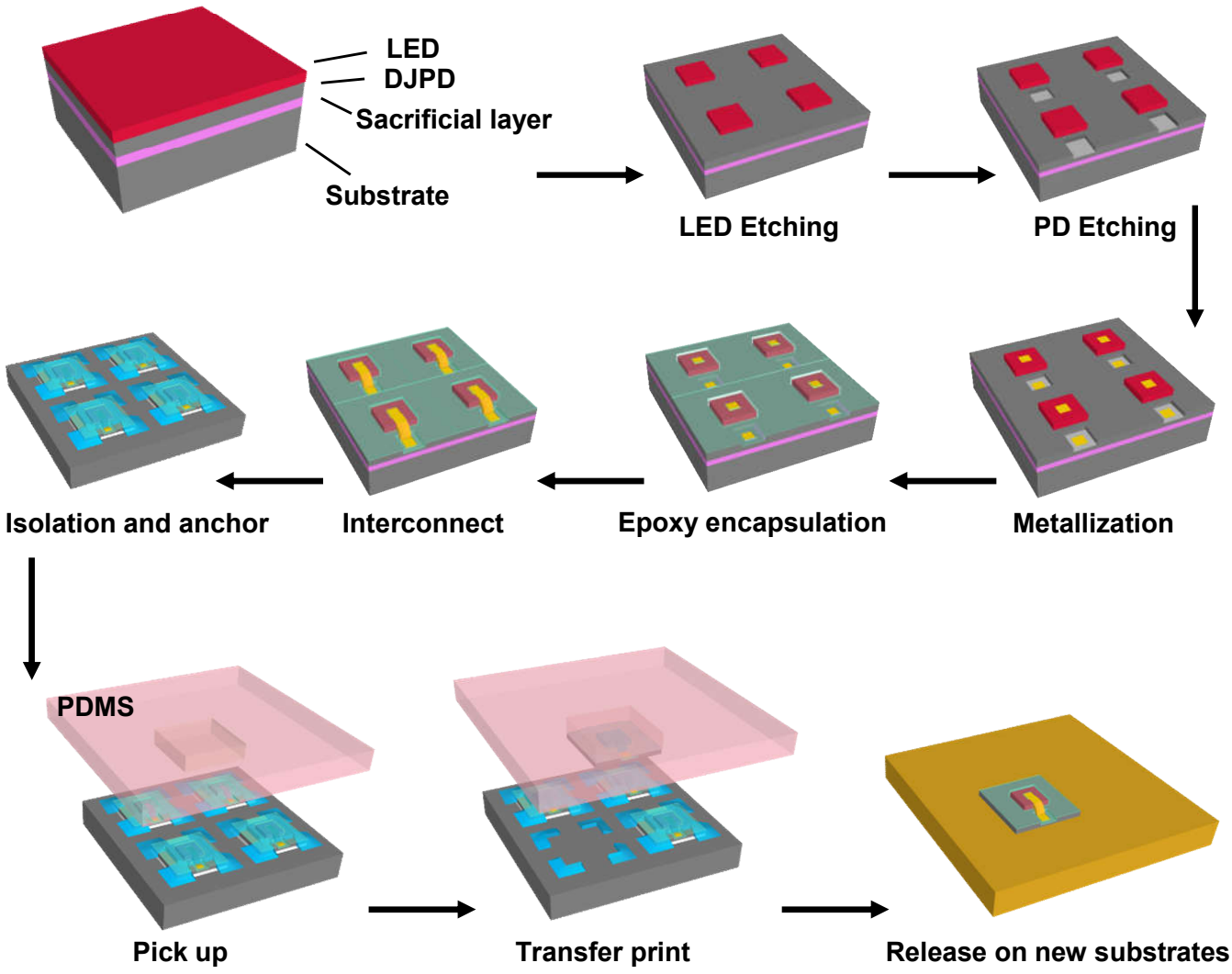

Figure S5. Schematic illustration of processing flow for the upconversion device fabrication, including LED etching, PD etching, metallization, SU-8 encapsulation, anchoring, sacrificial layer release and the transfer printing.

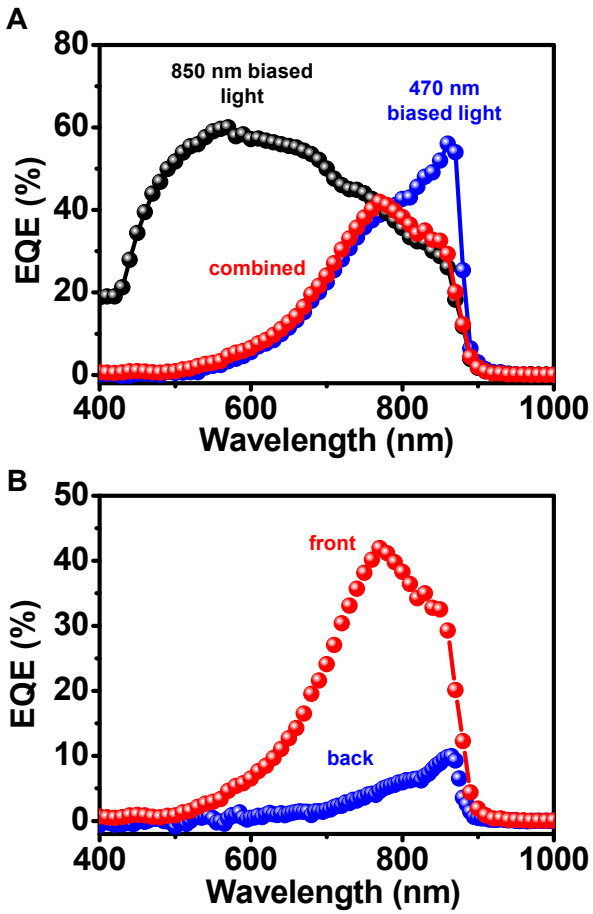

Figure S6. (**A**) Measured EQE spectra of the two subcells in the GaAs DJPD, with each subcell saturated with 850 nm and 473 nm light respectively, and the overlapping curve represents the EQE of the DJPD. (**B**) Measured EQE spectra of the GaAs DJPD under frontside and backside illumination. The low EQE under backside illumination is due to the optical loss at the thick bottom GaAs contact layer, as well as the unmatched currents between top and bottom cells.

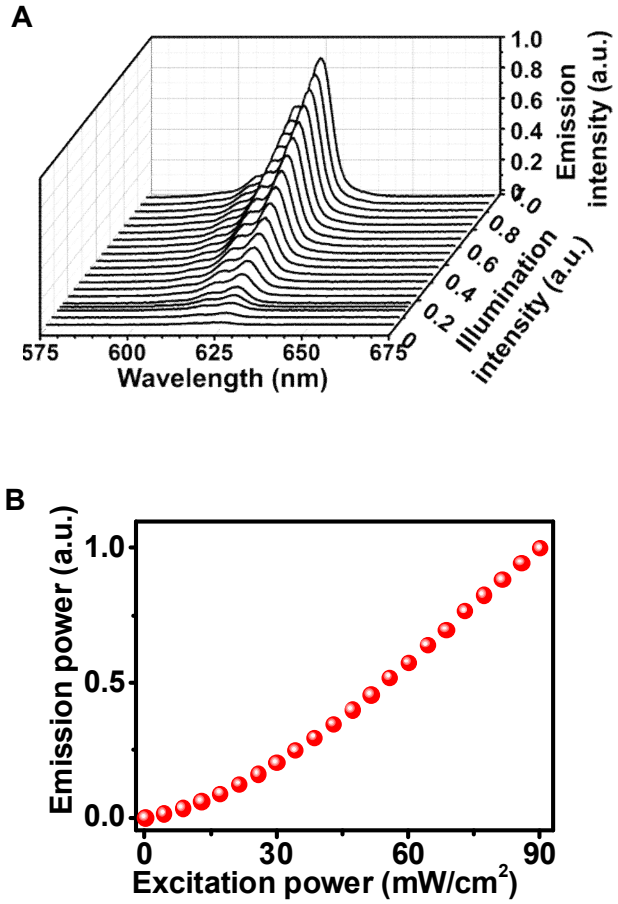

Figure S7. (**A**) Emission spectra of the IR-to-red upconversion device under IR excitation (808 nm) with various illumination intensity. (**B**) The relation of the excitation and emission power.

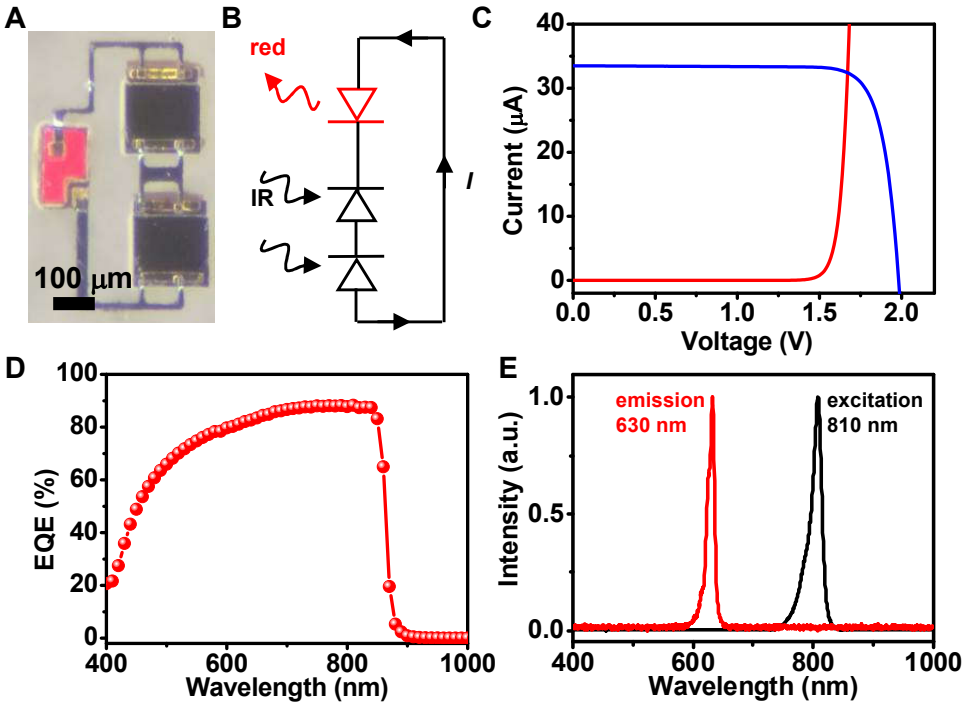

Figure S8. (**A**) Microscopic image of a fabricated IR-to-red upconversion system, with thin-film devices (a red InGaP LED and two single-junction GaAs PDs) transferred on polyimide and interconnected in series. (**B**) Operational principle of the integrated upconversion design. (**C**) Current–voltage curves for the red InGaP LED and the two serially connected GaAs PDs, measured independently. (**D**) EQE spectrum of a single-junction GaAs PD. (**E**) Spectra of excitation (810 nm) and emission (630 nm) of the integrated system, demonstrating IR-to-red upconversion.

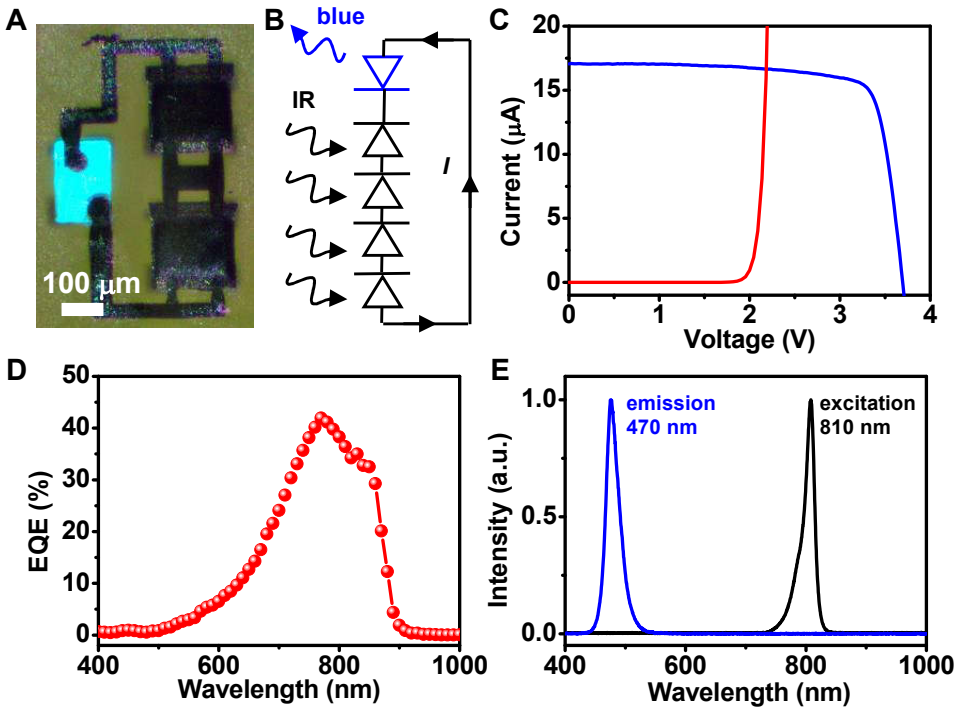

Figure S9. (**A**) Microscopic image of a fabricated IR-to-blue upconversion system, with thin-film devices (a blue InGaN LED and two double-junction GaAs PDs) transferred on polyimide and interconnected in series. (**B**) Operational principle of the integrated upconversion design. (**C**) Current–voltage curves for the blue InGaN LED and the two serially connected GaAs DJPDs, measured independently. (**D**) EQE spectrum of a double-junction GaAs PD. (**E**) Spectra of excitation (810 nm) and emission (470 nm) of the integrated system, demonstrating IR-to-blue upconversion.

Figure S10. Images of different symbols collected via an IR-to-red upconversion device array under patterned IR illumination.

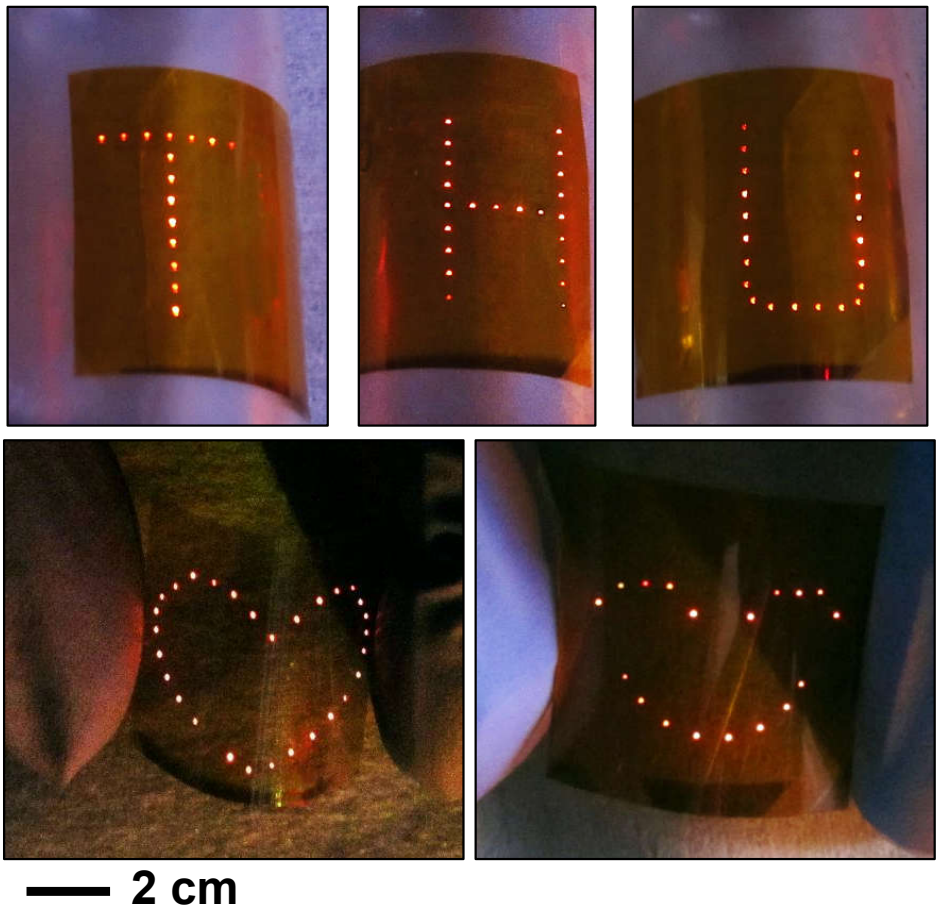

Figure S11. Images of different patterns formed by upconversion devices printed on 50 μm thick polyimide films under uniform IR illumination.

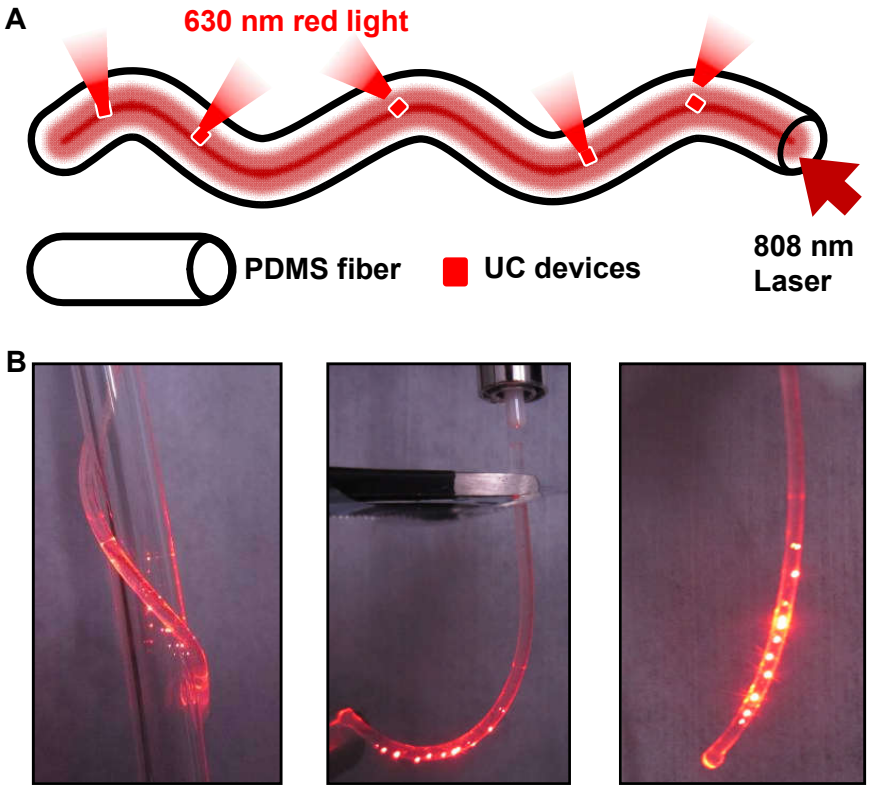

Figure S12. (**A**) Schematic illustration and (**B**) photographs showing microscale upconversion devices integrated with PDMS fibers with guided IR light.

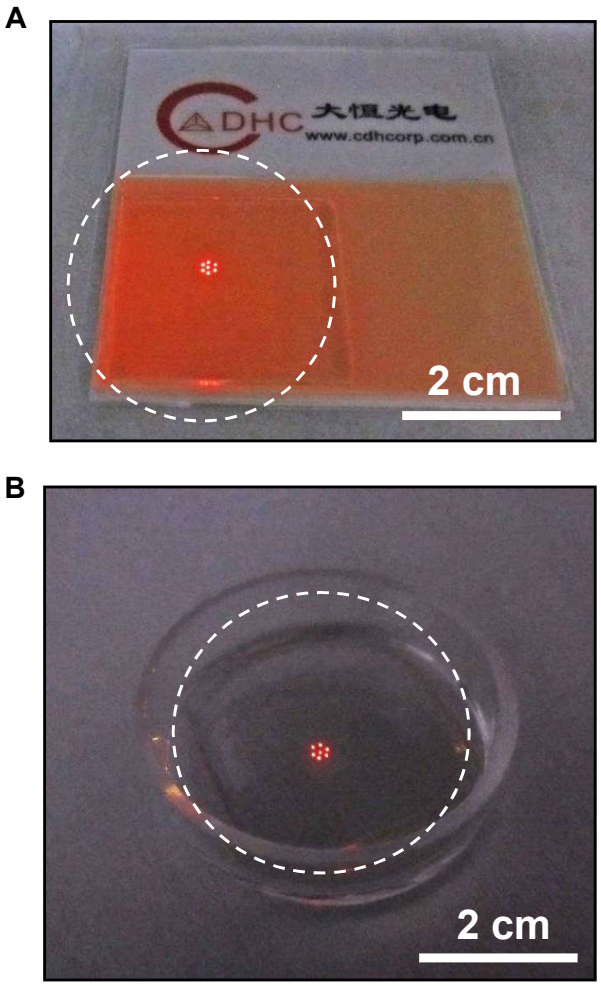

Figure S13. Photograph of some microscale upconversion devices printed on the glass (**A**) above a commercial upconversion infrared sensitive card (CaS:Ce,Sm, excitation: 800–1200 nm, emssion 585 nm, Daheng New Epoch Technology Inc.) (*Ref. 7*) and (**B**) below the $NaYF_4$:Yb,Er@$NaYF_4$:Yb@$NaNdF_4$:Yb core/shell/shell upconversion nanoparticles (*Ref. 8*) in $CHCl_3$ solution (excitation: 808 nm, emssion 550 nm). The IR illumination power density is 40 mW/cm^2, with irradiate area represented by the white dash circles. Under such IR illumination power, light emissions from CaS:Ce, Sm and $NaYF_4$:Yb,Er@$NaYF_4$:Yb@$NaNdF_4$:Yb nanoparticles are much weaker than that from our devices and difficult to capture using a camera.

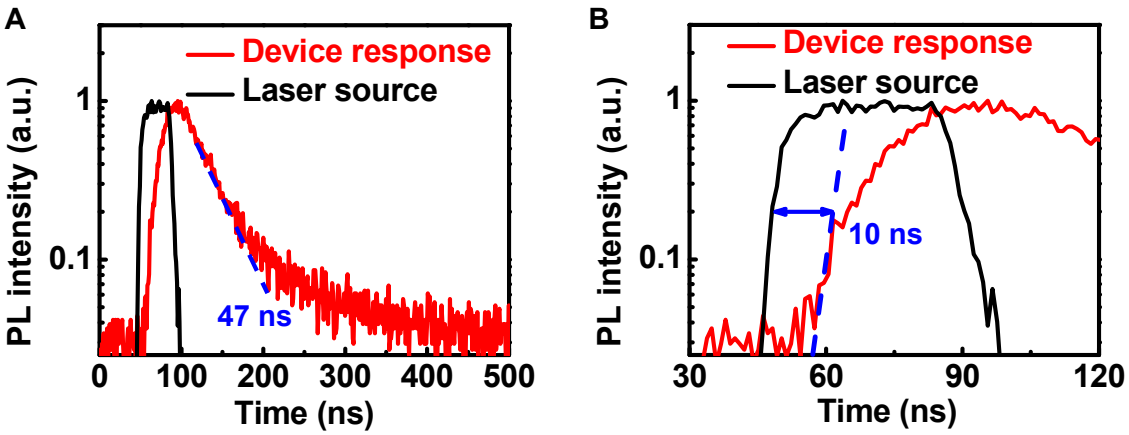

Figure S14. (**A**) PL decay of of the upconversion device (red curve), indicating a decay lifetime of 47 ns. The 785 nm IR laser source (black curve) has a pulse width of 30 ns. (**B**) A zoomed view of **a,** showing a response time of the rise of luminescence is about 10 ns.

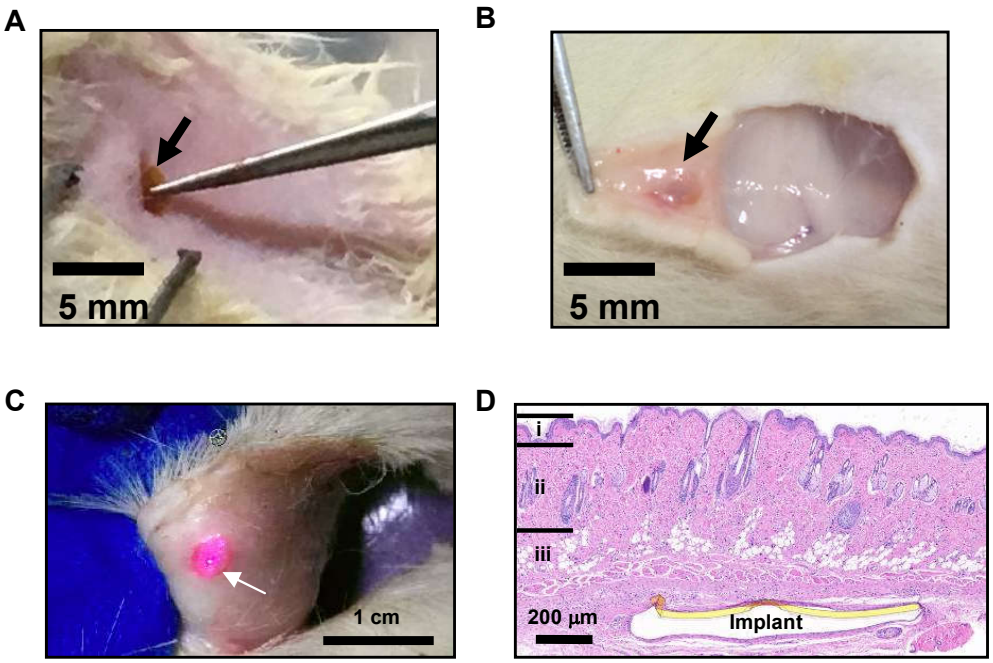

Figure S15. (**A**) Photograph of the subcutaneous implantation process in Sprague-Dawley (SD) rat with the encapsulated upconversion device on a polyimide (PI) film. (**B**) Photograph of the subcutaneous region with the implants after 1 weeks implantation, without obvious signs of the infection or inflammation. **(C)** Image of an encapsulated device implanted subcutaneously that can still exhibit IR-to-red emission after 3 weeks. **(D)** Histological sections stained with hematoxylin and eosin (H&E) of the subcutaneous tissue around the implanted devices. Indicated are the epithelium (i), the dermis (ii) and the hypodermis (iii).

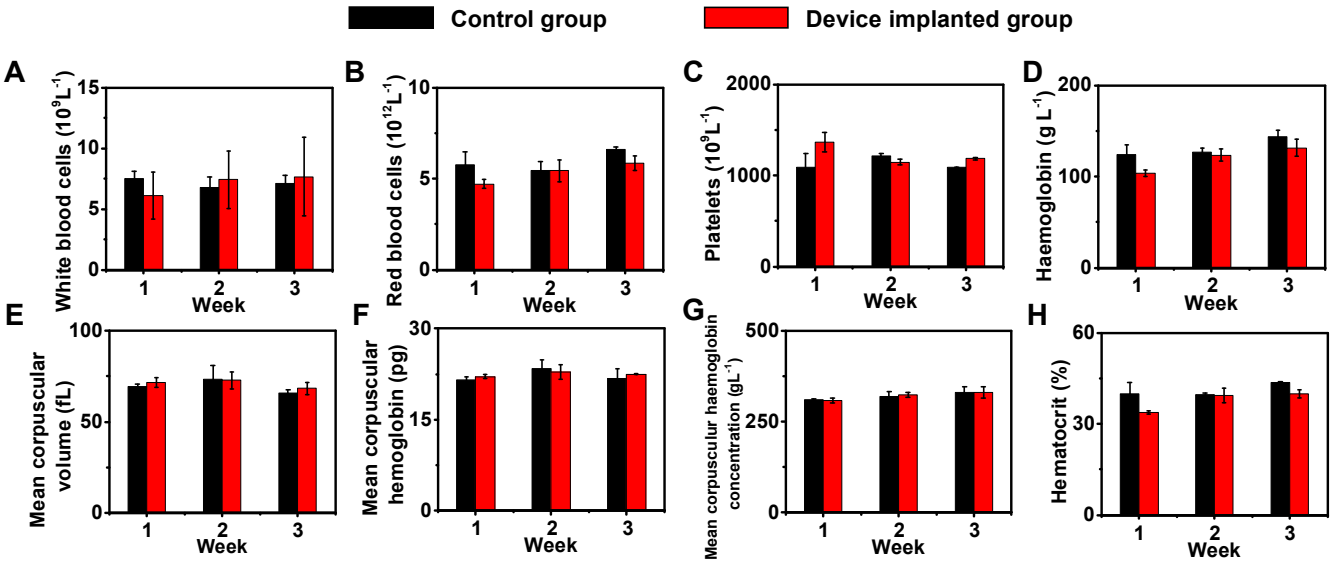

Figure S16. Time-course changes (3 weeks) of (**A**) white blood cells, (**B**) red blood cells, (**C**) platelets, (**D**) haemoglobin, (**E**) mean corpuscular volume, (**F**) mean corpuscular haemoglobin, (**G**) mean corpuscular haemoglobin concentration and (**H**) haematocrit from the control group (SD rats only have incisions without implants) and the group with implanted upconversion devices. Error bars indicate s.d. (n=3).

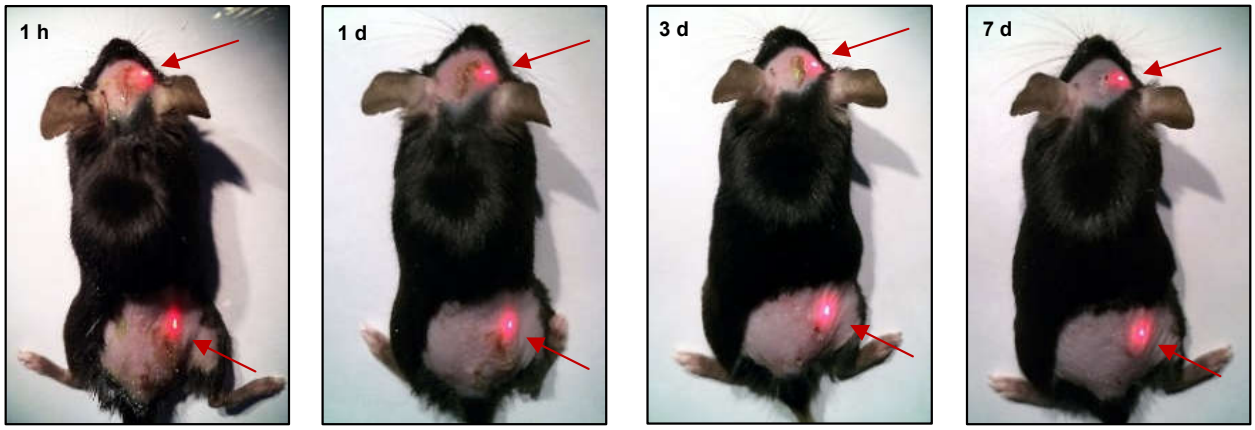

Figure S17. Luminance stability of the implanted upconversion devices in C57BL/6N mouse within 7 days.

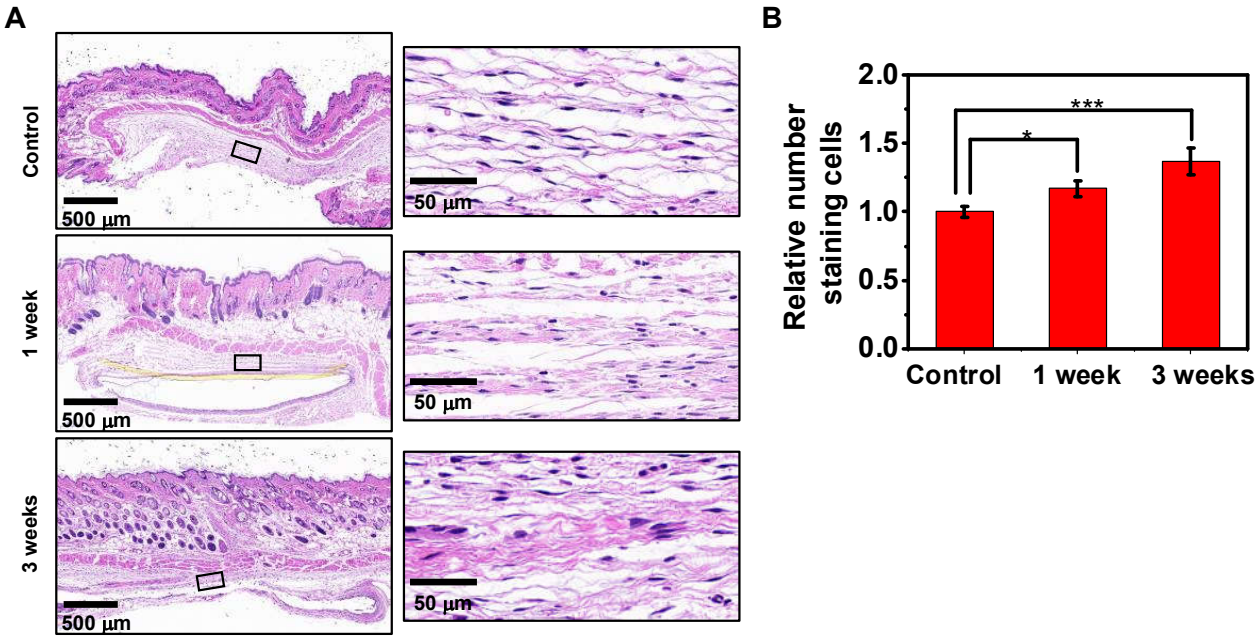

Figure S18. (A) Histological sections stained with hematoxylin and eosin (H&E) of the subcutaneous tissue around the implanted devices after 1 and 3 weeks in C57 black 6 (C57BL/6N) mice. (B) Analysis of relative immune cells after 1 and 3 weeks, respectively compared to the control group from H&E stained images. (n = 3 mice for each groups). *P<0.05, ***P<0.001, t-test.

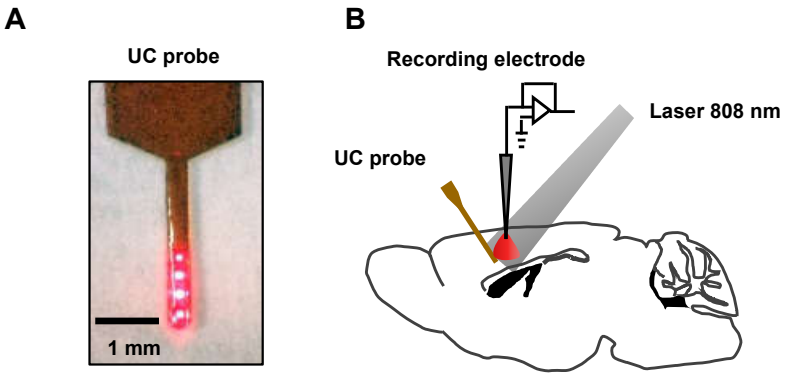

Figure S19. (A) Photograph of the upconversion devices transferred on the polyimide film probe. (B) Experimental diagram of stimulating Camk2a neurons and local field potential (LFP) recording in primary somatosensory cortex (S1) region.

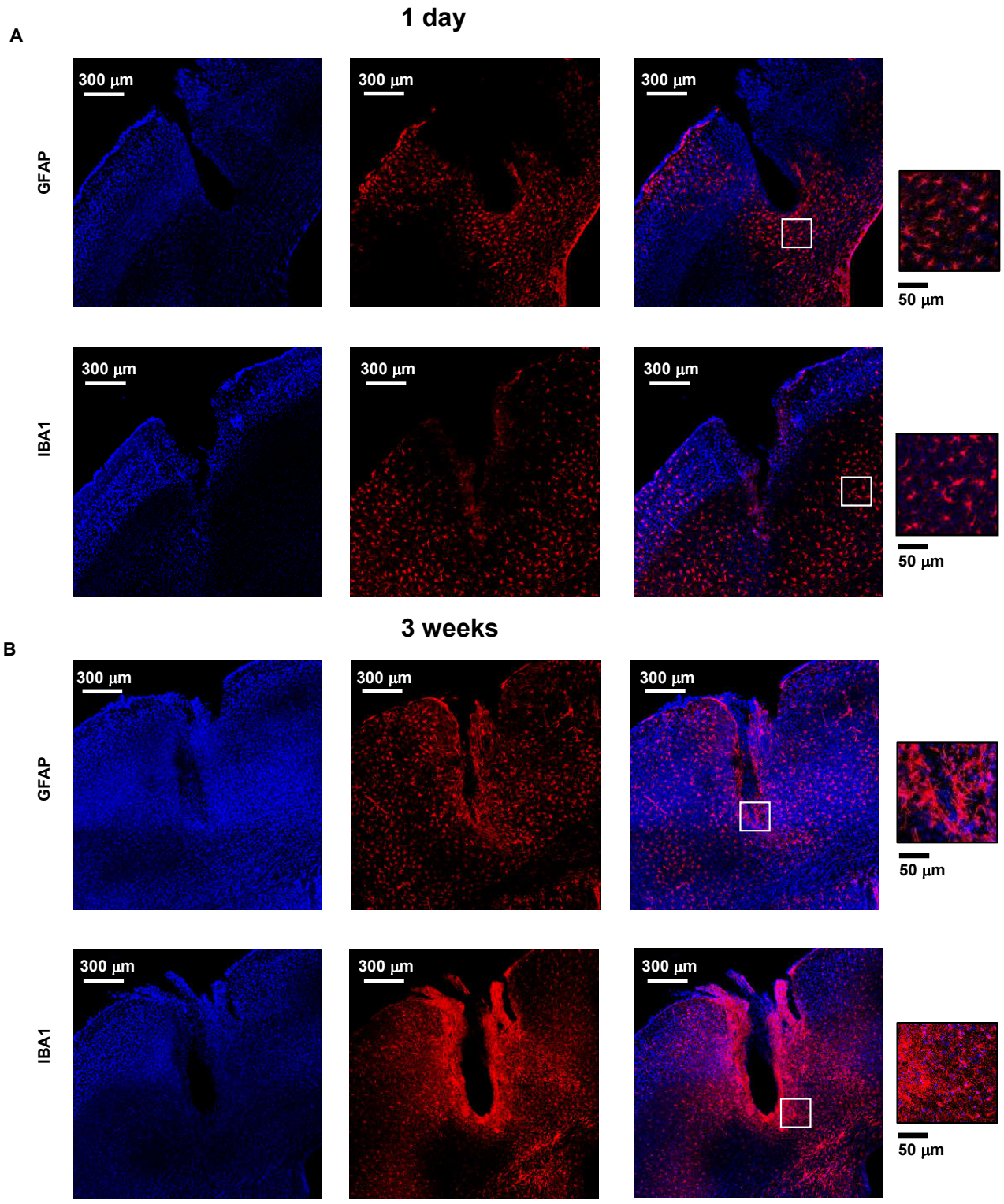

Figure S20. Confocal images of the implanted upconversion devices probe in primary somatosensory cortex (S1) regions, stained for Iba1+ microglia and GFAP+ astrocytes, after (A) 1 day and (B) 3 weeks, respectively.

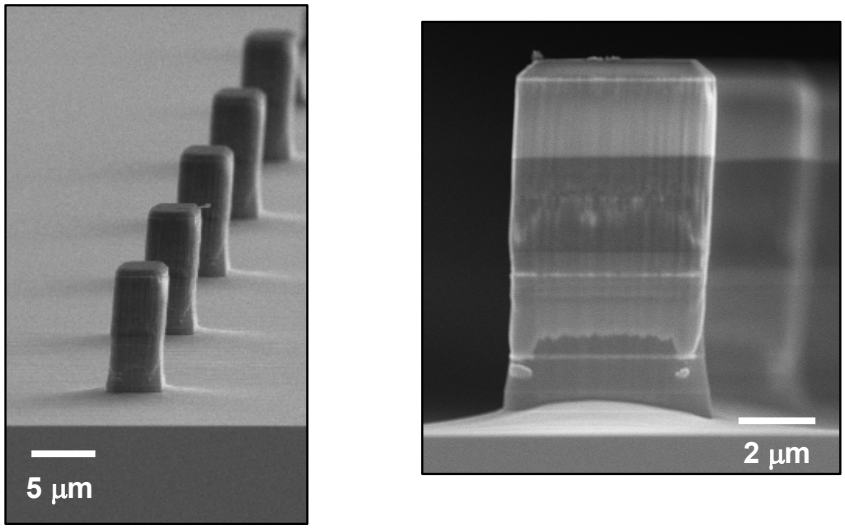

Figure S21. SEM images of the microscale (< 5 μm) upconversion structures by the ICP-RIE process.

Table S1. Epitaxial structure of the integrated IR-to-red upconversion device on a GaAs wafer. The structure of the IR-to-yellow upconversion device is similar, except that the LED part uses InAlP/InAlGaP MQWs and the DBR is optimized for yellow emission.

materials	thickness (nm)	doping (cm^{-3})	dopant	
p++ GaP contact	200	1e20	C	**InGaP red LED**
p+ GaP window	2000	5e18	Mg	
p InAlP	800	1e18	Mg	
InAlP / InGaP MQWs	200	-	-	
n InAlP	200	8e17	Si	
$In_{0.5}Al_{0.5}P$ / $In_{0.5}Al_{0.25}Ga_{0.25}P$ DBR 12 loops	1200	3e18	Si	**DBR**
n+ GaAs contact	700	6e18	Si	**ohmic contact**
n+ InGaP window	30	2e18	Si	**GaAs PD cell 1**
n+ GaAs emitter	100	2e18	Si	
p- GaAs base	450	1e17	Zn	
p+ $Al_{0.3}Ga_{0.7}As$ BSF	100	5e18	Mg	
p++ GaAs tunnel junction	11	8e19	C	**tunnel junction**
n++ GaAs tunnel junction	11	9e18	Se	
n+ $Al_{0.3}Ga_{0.7}As$ window	30	2e18	Si	**GaAs PD cell 2**
n+ GaAs emitter	100	2e18	Si	
p- GaAs base	1500	1e17	Zn	
p+ InGaP BSF	100	1e18	Mg	
p+ GaAs contact	1000	5e18	Mg	**sacrificial layer**
$Al_{0.95}Ga_{0.05}As$ sacrifacial	500	-	-	
GaAs substrate	-	-	-	

Table S2. Epitaxial structure of the GaAs wafer with the InGaP red LED.

materials	thickness (nm)	doping (cm^{-3})	dopant	
p++ GaP contact	200	1e20	C	**InGaP red LED**
p+ GaP window	2000	5e18	Mg	
p InAlP	800	1e18	Mg	
InAlP / InGaP MQWs	200	-	-	
n InAlP	200	8e17	Si	
$In_{0.5}Al_{0.5}P$ / $In_{0.5}Al_{0.25}Ga_{0.25}P$ DBR 12 loops	1200	3e18	Si	**DBR**
n+ GaAs contact	1000	6e18	Si	**ohmic contact**
$Al_{0.95}Ga_{0.05}As$ sacrifacial	500	-	-	**sacrificial layer**
GaAs substrate	-	-	-	

Table S3. Epitaxial structure of the GaAs wafer with the GaAs double-junction photodiode.

materials	thickness (nm)	doping (cm^{-3})	dopant	
n+ GaAs contact	200	6e18	Si	**ohmic contact**
n+ InGaP window	30	2e18	Si	**GaAs PD cell 1**
n+ GaAs emitter	100	2e18	Si	
p- GaAs base	450	1e17	Zn	
p+ $Al_{0.3}Ga_{0.7}As$ BSF	100	5e18	Mg	
p++ GaAs tunnel junction	11	8e19	C	**tunnel junction**
n++ GaAs tunnel junction	11	9e18	Se	
n+ $Al_{0.3}Ga_{0.7}As$ window	30	2e18	Si	**GaAs PD cell 2**
n+ GaAs emitter	100	2e18	Si	
p- GaAs base	1500	1e17	Zn	
p+ InGaP BSF	100	1e18	Mg	
p+ GaAs contact	1000	5e18	Mg	
$Al_{0.95}Ga_{0.05}As$ sacrifacial	500	-	-	**sacrificial layer**
GaAs substrate	-	-	-	

Table S4. Epitaxial structure of the GaAs wafer with the GaAs single-junction photodiode.

materials	thickness (nm)	doping (cm^{-3})	dopant	
n+ GaAs contact	200	6e18	Si	**ohmic contact**
n+ InGaP window	30	2e18	Si	
n+ GaAs emitter	100	2e18	Si	
p- GaAs base	2500	1e17	Zn	**GaAs PD cell**
p+ $Al_{0.3}Ga_{0.7}As$ BSF	100	5e18	Mg	
p+ GaAs contact	1000	5e18	Mg	
$Al_{0.95}Ga_{0.05}As$ sacrifacial	500	-	-	**sacrificial layer**
GaAs substrate	-	-	-	

Table S5. Comparison of performance between the IR-to-red upconversion device based on this work and the upconverting material $NaYF_4$:Yb^{3+}, Er^{3+} (Reference: F. Zhang, *Photon Upconversion Nanomaterials*, Springer, 2015).

	Upconversion device (this work)	$NaYF_4$:Yb^{3+}, Er^{3+}
efficiency	1.5%	0.001%–2% (depending on excitation intensity)
linearity	linear	non-linear
excitation	broad band (400–900 nm)	narrow band (980 nm, 1550 nm, …)
emission	monochromic (630 nm)	polychromic (400 nm, 520 nm, 550 nm, 650 nm, …)
PL lifetime	47 ns	0.1–100 ms

Movie S1. Video for a collection of microscale upconversion devices immersed in PBS

Movie S2. Video for a collection of microscale upconversion devices flowing in fluids.

Movie S3. Video for a freely behaving mouse with upconversion devices implanted subdermally on the head under the IR illumination.